Phase transitions, Dirac and Weyl semimetal states in $Mn_{1-x}Ge_xBi_2Te_4$

A.M. Shikin[1,*], N.L. Zaitsev[1,2], T.P. Estyunina[1], D.A. Estyunin[1], A.G. Rybkin[1], D.A. Glazkova[1], I.I. Klimovskikh[3], A.V. Eryzhenkov[1], K.A. Kokh[1,5], V.A. Golyashov[1,4], O.E. Tereshchenko[1,4], S. Ideta[6], Y. Miyai[6], Y. Kumar[6], T. Iwata[7,8], T. Kosa[7], K. Kuroda[7,8,9], K. Shimada[6], and A.V. Tarasov[1]

[1]Saint Petersburg State University, St. Petersburg 198504, Russia
[2]Institute of Molecule and Crystal Physics, Subdivision of the Ufa Federal Research Centre of the Russian Academy of Sciences, Ufa 450075, Russia
[3]Donostia International Physics Center (DIPC), 20018 Donostia-San Sebastián, Basque Country, Spain
[4]Rzhanov Institute of Semiconductor Physics, Siberian Branch, Russian Academy of Sciences, Novosibirsk 630090, Russia
[5]Sobolev Institute of Geology and Mineralogy, Siberian Branch, Russian Academy of Sciences, Novosibirsk 630090, Russia
[6]Research Institute for Synchrotron Radiation Science, Hiroshima University, Hiroshima 739-0046, Japan
[7]Graduate School of Advanced Science and Engineering, Hiroshima University, Higashi-Hiroshima 739-8526, Japan
[8]International Institute for Sustainability with Knotted Chiral Meta Matter (WPI-SKCM^2), Hiroshima University, Higashi-Hiroshima 739-8526, Japan
[9]Research Institute for Semiconductor Engineering, Hiroshima University, Higashi-Hiroshima 739-8527, Japan
[*]ashikin@inbox.ru

ABSTRACT

Using angle-resolved photoemission spectroscopy (ARPES) and density functional theory (DFT), an experimental and theoretical study of changes in the electronic structure (dispersion dependencies) and corresponding modification of the energy band gap at the Dirac point (DP) for topological insulator (TI) $Mn_{1-x}Ge_xBi_2Te_4$ have been carried out with gradual replacement of magnetic Mn atoms by non-magnetic Ge atoms when concentration of the latter was varied from 10% to 75%. It was shown that when Ge concentration increases then the bulk band gap decreases and reaches zero plateau in the concentration range of 45%–60% while trivial surface states (TrSS) are present and exhibit an energy splitting of 100 and 70 meV in different types of measurements. It was also shown that TSS disappear from the measured band dispersions at a Ge concentration of about 40%. DFT calculations of $Mn_{1-x}Ge_xBi_2Te_4$ band structure were carried out to identify the nature of observed band dispersion features and to analyze a possibility of magnetic Weyl semimetal state formation in this system. These calculations were performed for both antiferromagnetic (AFM) and ferromagnetic (FM) ordering types while the spin-orbit coupling (SOC) strength was varied or a strain (compression or tension) along the c-axis was applied. Calculations show that two different series of topological phase transitions (TPTs) may be implemented in this system depending on the magnetic ordering. At AFM ordering transition between TI and trivial insulator phase goes through the Dirac semimetal state, whereas for FM phase such route admits three intermediate states instead of one (TI — Dirac semimetal — Weyl semimetal — Dirac semimetal — trivial insulator). Weyl points that form in FM system along the ΓZ direction annihilate when either the SOC strength decreases or a sufficient tensile strain is applied, which is accompanied by the corresponding TPTs. Model calculations of local magnetic ordering influence in AFM $Mn_{1-x}Ge_xBi_2Te_4$ was carried out by alternating Mn layers and Ge-doped layers and showed that the magnetic Weyl semimetal state in this system is reachable at a Ge concentration of approximately 40% without application of any external magnetic fields.

Introduction

Magnetic topological insulators (TIs) have attracted significant interest from researchers over the past 10 years, both from a fundamental perspective (see, for example,[1–6]) and due to their high prospects for effective use in modern topological antiferromagnetic spintronics and magnetoelectronics (see, for example,[7,8]). Recently, a series of intrinsic magnetically-ordered TIs from the $MnBi_2Te_4$ family have been successfully synthesized and studied (see, for example,[9–23]). These materials, due to the ordering of magnetic atoms and their increased concentrations (compared to magnetically doped TIs), are characterized by an enhanced interaction between magnetism and topology. This leads to significantly higher temperatures for realizing

the quantum anomalous Hall effect (QAHE) and other quantum topological effects compared to magnetically doped TIs[24–28]. For thin layers of $MnBi_2Te_4$, QAHE has been observed at a temperature of 1.4 K. This temperature increases to 6.5 K when transitioning from antiferromagnetic (AFM) to ferromagnetic (FM) interlayer coupling under an applied external magnetic field[24]. Therefore, the search for $MnBi_2Te_4$-based compounds with strong spin-orbit coupling (SOC) and FM interlayer coupling is a promising area for achieving "high-temperature" QAHE. Additionally, this TI is characterized by an increased energy gap at the Dirac point (DP) in topological surface states (TSS). This energy gap can vary widely, from 70–90 meV to several meV[10–20], and even to gapless dispersions[29–31], potentially making it possible to control the aforementioned topological quantum properties. One possible method to change the gap size and reach the region of topological phase transition (TPT) from the topological to the trivial phase is the controlled replacement of heavy elements with lighter ones, such as replacing Te with Se or Bi with Sb[20,32–34]. In this case, the system approaches a state close to the TPT, where an axion-like state (with a non-zero gap at the TPT point)[20] and the corresponding topological magneto-electric (ME) effect can be realized.

However, there is another possibility of modulating the energy gap at the DP and reaching the TPT point through the partial replacement of Mn atoms with IV-group elements (Ge, Sn, Pb)[35–41]. In Refs[35–37], it was shown that when Mn is replaced by Ge, Sn, or Pb atoms in the $Mn_{1-x}A_xBi_2Te_4$ ($A = Ge, Sn, Pb$) compounds, the bulk band gap decreases with an increase in the concentration of the substituting atoms. The gap decreases to practically zero at substituting element concentrations of 40–50%, with a possible transition from the topological state to the Weyl semimetal (WSM) state. Furthermore, there is a potential reverse transition to a state similar to Mn-doped [Ge,Pb,Sn]Bi_2Te_4.

At the same time, for the $Mn_{1-x}[Ge, Sn, Pb]_xBi_2Te_4$ compounds, it was revealed that with an increase in the concentration of non-magnetic atoms, the magnetic properties also change. The Néel temperature decreases from 24.5 K to 10–15 K when Mn atoms are replaced by Ge, Pb, or Sn atoms at concentrations of 50–80%, and further down to 5 K. Additionally, the spin-flop transition threshold is reduced from 7 Tesla to 1–2 Tesla, and further to 0.5 Tesla[42]. This means that, while the remagnetization in $MnBi_2Te_4$ and the corresponding transition from the AFM to FM state requires the application of a magnetic field of approximately 7 Tesla, systems with a 50% replacement of the magnetic atom by non-magnetic elements require only 1–1.5 Tesla. For higher concentrations, the remagnetization threshold decreases further to 0.5 Tesla. The study of the transition to the FM phase is very important, especially from the perspective of transitioning to the WSM state with its unique properties. Therefore, investigating the possibility of realizing the magnetic WSM state is a significant and challenging scientific task, particularly for TI $Mn_{1-x}A_xBi_2Te_4$.

It should be noted that interest in the study of Weyl semimetals (including magnetic ones) has increased significantly in recent years. These materials are characterized by a topological invariant and the corresponding chiral charge, as well as unique features in their electronic structure and formation conditions. This interest is due to the unique properties of Weyl semimetals, such as the anomalous spin Hall effect, the chiral anomaly, chiral magnetic effects, and large (negative) magnetoresistance. Additionally, Weyl semimetals are promising for the analysis of Majorana fermion stabilization in unconventional superconductivity. They also offer the possibility of using the solid-state black-hole-horizon analogy, which emerges at the Lifshitz transition between different WSM phases, in astrophysics (see, for example,[43–47] and references therein). In this context, the formed Weyl nodes (Weyl points) of opposite chirality are singularities (sources) of Berry curvature (or monopoles of Berry flux), which can be regarded as analogs of the magnetic monopole and antimonopole in k–space[43,45,46].

As for $Mn_{1-x}A_xBi_2Te_4$, it was shown in[6,13,43,44,48] that a necessary condition for the formation of the WSM state in compounds from the $MnBi_2Te_4$ TI family is the presence of FM-type interaction in the system. Therefore, to analyze the possibility of forming the WSM state (as well as a Dirac semimetal), this work presents a comparative analysis of changes in the electronic structure of the $Mn_{1-x}Ge_xBi_2Te_4$ system with AFM and FM interactions. This analysis was carried out under the gradual replacement of Mn atoms (a magnetic metal) with Ge atoms (a nonmagnetic element). In this study, Ge atoms were selected as the substituent (from group IV elements Ge, Sn, Pb) due to their smallest atomic size in this group. This choice was made to minimize changes in the crystal parameters of $MnBi_2Te_4$ when replacing Mn atoms with Ge atoms across a wide range of concentrations.

In this work, we present and analyze the results of theoretical calculations of the electronic structure of $Mn_{1-x}Ge_xBi_2Te_4$ with varying Ge concentrations using the DFT method, in comparison with experimental photoemission studies. Additionally, this work presents the results of modeling the potential implementation of a WSM (and corresponding changes in the electronic structure) in $Mn_{1-x}Ge_xBi_2Te_4$ systems with AFM and FM interactions. This modeling involves modulating the SOC strength and interatomic (interplanar) distance, assuming various influences on the analyzed system. The details of the TPT from the TI state (characteristic of $MnBi_2Te_4$) to the trivial state, either through the Dirac semimetal (DSM) phase or the DSM–WSM–DSM sequence, will be presented and analyzed. Factors influencing the implementation and specifics of such topological phase transitions (TPTs) will also be identified. Finally, this study proposes the idea of a transition from the AFM TI to the WSM state directly in the initial AFM phase (without external remagnetization) by introducing local inhomogeneities in the AFM interaction through the gradual replacement of Mn atoms with Ge atoms in one Mn-layer.

Experimental Results

Fig. 1 (a1–a8) presents ARPES data at a photon energy of 21.2 eV for $Mn_{1-x}Ge_xBi_2Te_4$ with varying Ge concentrations, ranging from 12% to 90% relative to the initial Mn atom concentration in $MnBi_2Te_4$ (100%). At this photon energy, the ARPES data predominantly reflect bulk-derived states[37,49] and trivial surface states (TrSS)[49], providing insight into changes in the bulk bandgap size and the nearby valence and conduction bands (VB and CB) with increasing Ge concentrations. Notably, TSS located in the bulk band gap region at the $\bar{\Gamma}$-point are practically not visible in these measurements for $MnBi_2Te_4$. In the current work we do not study the detailed dependece of the gap on the k_z (or photon energy) and used only two photon energies ($h\nu = 21.2$ eV (Fig. 1) and 6.3 eV(Fig. 2)) for the separation of the contribution in the photoemission spectra of bulk states (and corresponding bulk energy gap variation), TSS and TrSS for analysis of tendention of their changes).

All of our experimentally measured samples exhibited n-doping due to the presence of Te vacancies and Te/Bi antisite defects, which are characteristic of the sample synthesis process (for comparison, see ref.[50]). The issue of reducing n-doping can be addressed by refining the sample synthesis technology, including the use of molecular beam epitaxy (MBE). For the related $MnBi_2Te_4$ topological insulator Bi_2Te_3, there are many established methods for shifting the Fermi level and obtaining compensated semiconductors. These methods could also be applicable to $MnBi_2Te_4$ (see, for example, ref.[51]).

The white lines in Fig. 1 (a1–a8) represent the energy distribution curves (EDC) for the electron density states, measured directly at the $\bar{\Gamma}$-point. These curves demonstrate changes in the bulk energy gap, considering contributions from TrSS and the bulk Bi-Te p_z states at the upper edge of the VB, as it will be detailed in the theoretical calculations below. Fig. 1 (b) shows the variation in the energy separation between the peak maxima in the EDC around the $\bar{\Gamma}$-point with increasing Ge concentration. The energy positions of the maxima on the EDC are indicated by horizontal white lines.

As the Ge concentration increases, the Ge-contributed states (as shown in Fig. 3 through theoretical calculations, primarily of surface character) significantly influenced by interactions with introduced Ge atoms, gradually emerge in the ARPES data. These states appear as "Rashba-like" states at the edges of the cone-like dispersions. Additionally, some smeared states energetically localized in the region near the original Dirac point appear in the spectra at Ge concentrations of 47–60% , which we attribute to the contribution of bulk states. They become more clearly observable within the region of the Dirac point in photoelectron spectra under laser excitation (refer to Fig. 2 below).

Analysis of the presented spectra reveals a gradual decrease in the initial bulk band gap size as Mn atoms are replaced by Ge atoms, observed up to concentrations of 47–60%. EDC at the $\bar{\Gamma}$-point at concentrations of 47–51% demonstrate a consistent measured gap (peak splitting) of about 70 meV. Concurrently, a less pronounced cone of bulk states emerges within this gap (energy state splitting), depicted by shaded areas in Fig. 1 (a5–a7), which are more clearly visible at the detailed representations in Fig. 1 (c1, c2, c3). These states, along with Rashba-like states, shift towards the initial DP, tending to form an apparent zero band gap at these concentrations. The apparent zero gap sizes at Ge concentrations between 47 and 60% are marked by crosses and by grey region in Fig. 1 (b).

The states exhibiting an energy splitting of about 70 meV (clearly discernible in the EDC) are likely formed due to the inclusion of TrSS (see the analysis of the theoretical calculations later, in Fig. 3). Moreover, the formed Rashba-like states gradually shift towards higher binding energies with increasing Ge concentration, concurrently hybridizing with cone-like states from the CB. As demonstrated in the theoretical calculations, just this hybridization leads to the formation and constancy of the observed 70 meV state splitting at Ge concentrations of 47 and 51%. At concentrations around 60%, the Rashba-like states intersect with lower cone states, eventually resulting in the formation of the apparent zero band gap. As the Ge concentration approaches 90%, the states of the upper cone shift back towards lower binding energies, again forming a pronounced band gap. The ARPES data then resemble those more characteristic of Mn-doped $GeBi_2Te_4$, featuring the bulk band gap and TSS branches in the region of their intersection with the edge of the VB (for comparison, see[36,37] for $GeBi_2Te_4$).

The observed decrease in the band gap, culminating in an apparent zero gap with increasing Ge concentration, and the formation of a plateau with a minimum band gap in the concentration range of 45–55%, followed by a transition to the electronic structure of Mn-doped $GeBi_2Te_4$ (at 90%), is consistent with previously reported data in the literature. This pattern has been observed both in systems where Mn atoms are replaced by Ge atoms[36,37], as well as for substitutions with other Group IV elements such as Sn[35] and Pb[38]. However, the underlying reason for the formation of the minimum band gap plateau has remained unclear until now. Here, we would like to note that the observation of a plateau at the near-zero value of the bulk band gap (as we will show later) confirms that topological phase transitions into Weyl and Dirac semimetal states are possible in the system under study. The second part of this work will focus on analyzing the possibility and conditions of transitioning to the Dirac and Weyl semimetallic phases. The starting point for this detailed analysis will be the experimental observation of the plateau with a near-zero gap, depending on the concentration of Ge atoms.

To identify the contribution of the TSSs to the electronic structures of the studied crystals, as well as other fine changes near the edges of the bulk bandgap caused by the increase in Ge concentration, we have performed measurements using high energy and angular resolution ARPES with laser photoexcitation ($h\nu = 6.3$ eV, see methods sections for details). This photon energy is well suited to resolve the TSS in the $MnBi_2Te_4$ family of materials[10,15–20]. In addition, laser radiation allows higher angular,

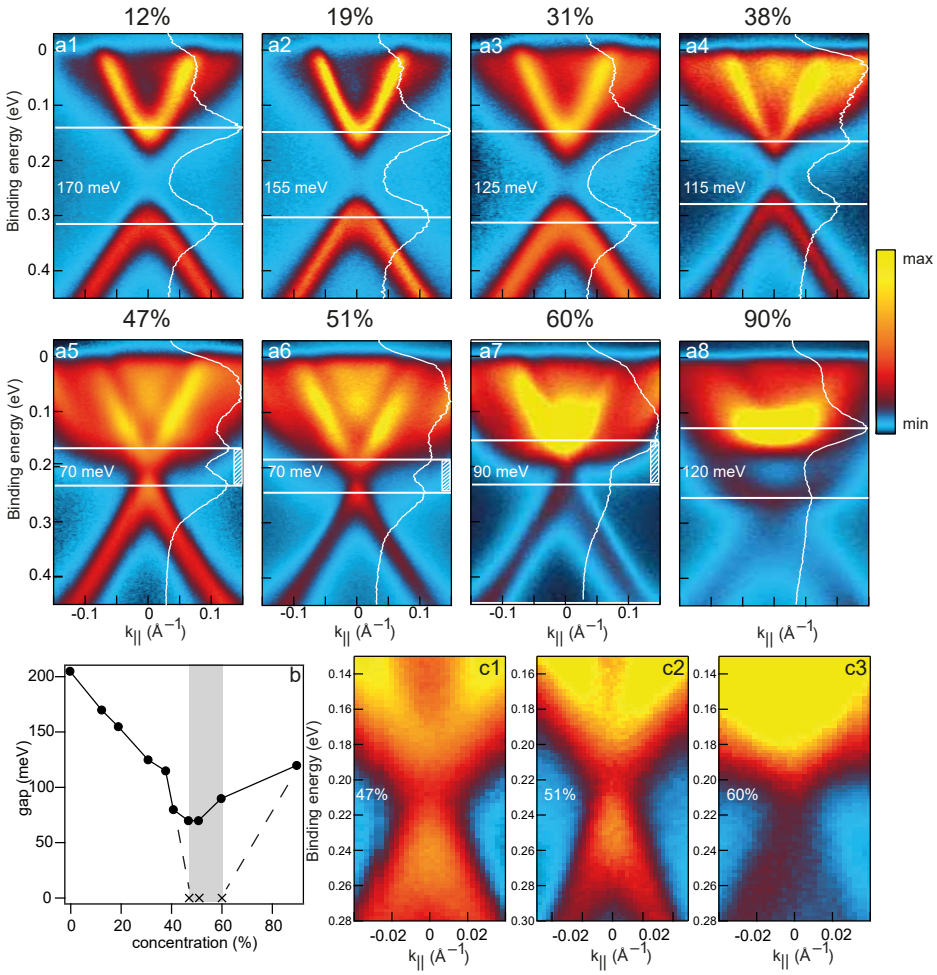

Figure 1. (**a1**–**a8**) ARPES data for $Mn_{1-x}Ge_xBi_2Te_4$ with Ge concentrations ranging from 12% to 90%, measured using a He lamp ($h\nu = 21.2$ eV). White lines represent EDCs at the $\bar{\Gamma}$-point. (**b**) Dependence of the band gap on Ge concentration, shown as the distance between peaks in the EDCs (solid line with dots) and the non-zero signal intensity between peaks for concentrations from 47% to 60% (dashed line with crosses). (**c1**–**c3**) Detailed view of the band dispersions near DP for Ge concentrations of 47%, 51%, and 60%.

spatial (spot size 5–10 μm) and energy resolutions (about 5 meV)[52,53].

Fig. 2(a1-a7) shows the experimental dispersions relations of $Mn_{1-x}Ge_xBi_2Te_4$ with Ge concentrations ranging from 12% to 90%. In Fig. 2(a1-a7), the dispersions are shown as N(E), and in Fig. 2(b1-b7), as d^2N/dE^2, for better visualization of the observed features. The presented dispersions are obtained by summing over all measured polarizations (s, p, c_+, c_-) of the exciting laser radiation for (a1–a4,a7) and over s,p-polarizations for (a5,a6). This was done to improve the signal-to-noise ratio, given the small differences in the measurement geometry.

Fig. 2(c1–c7) shows the corresponding EDC profiles at the $\bar{\Gamma}$-point, decomposed into spectral components to highlight the TSSs and the changes in energy splitting between different states of the CB and VB with varying Ge concentrations.

At low Ge concentrations, TSS branches, as well as the nearest states in the VB and CB, are clearly visible in the presented dispersion dependencies. In Fig. 2(a1), at a Ge concentration of 12% and a temperature of 16–18 K, the measured data shows the splitting of the Te p_z states in the CB and the (Bi-Te) p_z mixed states in the VB, localized in the regions of binding energies of 0.10–0.14 eV and 0.31–0.34 eV, respectively. The energy separation between these states in the CB and VB is indicated by horizontal green lines marked as Δ_2.

According to the literature, at temperatures below the Néel temperature (24.5–25.0 K for $MnBi_2Te_4$[10,11,15] and 25–26 K for 12% Ge[42]), the Te p_z states (due to magnetic ordering in the system) are energetically split (see Figs. 2(a1,b1) for Ge 12%). However, at temperatures above the Néel temperature, the magnitude of the splitting of these states decreases to zero, similar to the findings in[10,15,42].

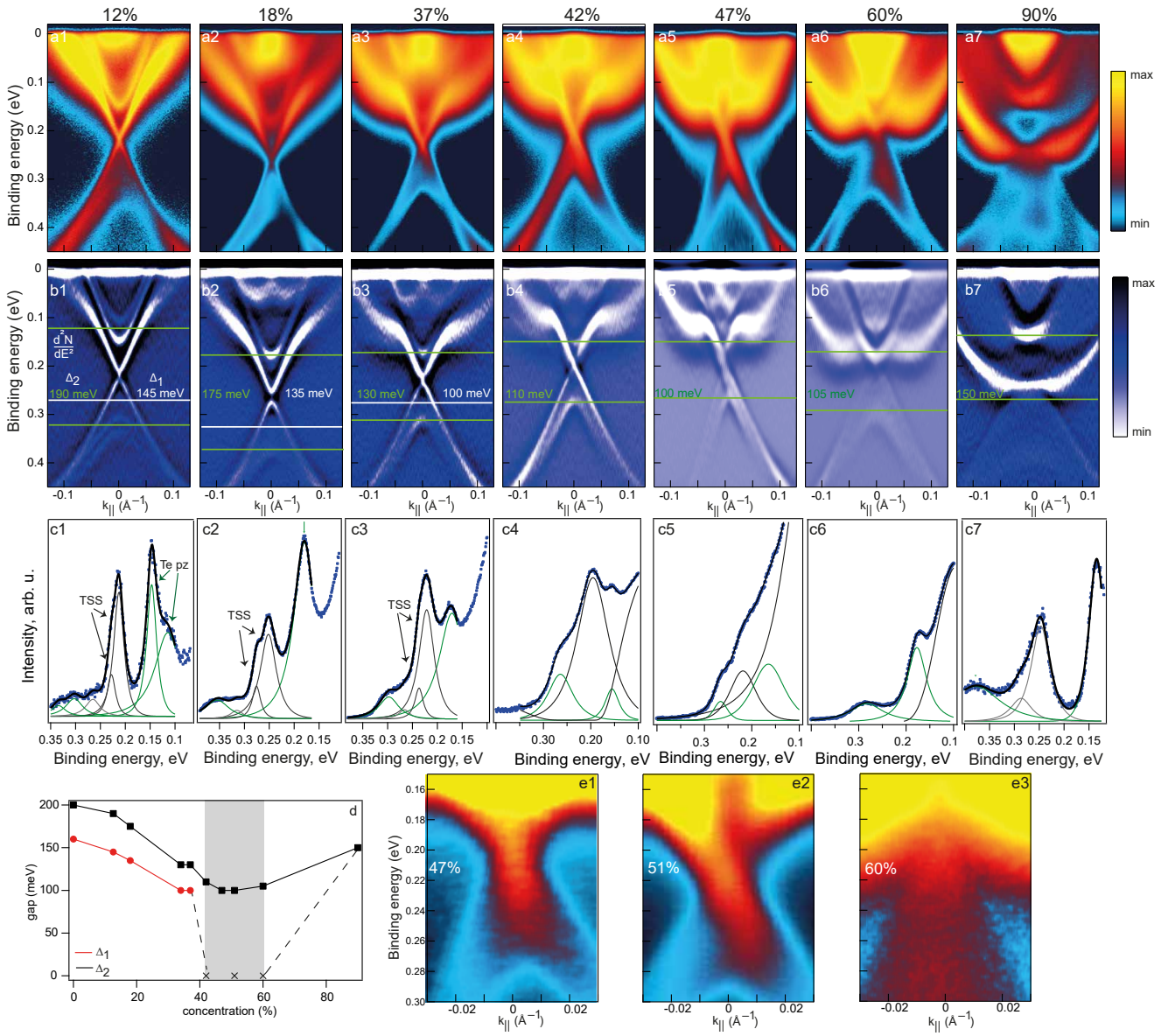

Figure 2. Experimental dispersion profiles obtained via high energy- and angle-resolution ARPES using laser radiation ($h\nu = 6.3$ eV) for $Mn_{1-x}Ge_xBi_2Te_4$ with Ge concentrations ranging from 12% to 90% are presented as follows: (**a1–a7**) in $N(E)$ format, (**b1–b7**) in d^2N/dE^2 format, and (**c1–c7**) the corresponding density of states profiles at the $\bar{\Gamma}$-point with decomposition into spectral components. (**d**) Dependence of the energy band gap size at the $\bar{\Gamma}$-point on the Ge concentration. Crosses indicate the formation of an apparent zero energy bulk gap at Ge concentrations between 42% and 60%. (**e1–e3**) Detailed representation of the dispersion dependencies ($N(E)$) for Ge concentrations between 47% and 60% using *s*-polarization of laser radiation in the vicinity of the initial DP at the $\bar{\Gamma}$-point.

The spectra for higher Ge concentrations in Fig. 2 were measured at temperatures above the Néel temperatures corresponding to these concentrations[42]. Therefore, the dispersions shown in Fig. 2 for higher Ge concentrations do not show the splitting of the Te p_z and (Bi-Te) p_z mixed states in the CB and VB (see also the decomposition of EDC into components in Fig. 2(c1–c3)).

To compare the change in separation between the Te p_z states in the CB and the (Bi-Te) p_z mixed states in the VB at different temperatures, horizontal lines corresponding to Δ_2 are drawn between the midpoints of the splittings occurring for these states. The magnitude of this state separation (shown in Fig. 2) was estimated for a Ge concentration of 12% as the average value between pairs of the top and bottom split state separations.

The measured dispersions in Fig. 2 reveal states near the upper part of the VB, close to the DP, at an energy of approximately

0.28 eV. These states likely include both the Bi p_z states at the VB edge and TrSS (as discussed further in the theoretical calculations). The corresponding transitions are labeled as Δ_1. It is plausible that the peaks observed in the EDC at the $\bar{\Gamma}$-point in Fig. 1 arise from a mixture of contributions from the (Bi-Te) p_z states in the VB and these TrSS, due to limited energy and spatial resolution. Consequently, the estimated sizes of the bulk band gap from Fig. 1 fall between the values of Δ_1 and Δ_2 depicted in Fig. 2. A more detailed analysis of these contributions will be provided later in the discussion of theoretical calculations.

Overall, the dispersions presented in Fig. 2 (as well as in Fig. 1) show a noticeable reduction in the state separations Δ_1 and Δ_2 with increasing Ge concentration. The variations in these state separations with Ge concentration, estimated from the decomposition of EDC, are illustrated in Fig. 2(d) using black and red circles, respectively. These state separations reach average values of approximately 100 meV within the concentration range of 42–51%, where their constancy is observed, consistent with the trends in Fig. 1.

It should be noted that the TSSs are clearly visible in the high energy- and angle-resolution ARPES data only up to a Ge concentration of approximately 37–42%. The energy splitting for the TSSs in the presented data is mainly in the range of 10–15 meV. However, at a Ge concentration of 47%, the TSSs are no longer visible in the measured data. In the region of the DP, the contribution of the bulk Ge-contributed states is more likely to appear, leading to the formation of an apparent zero energy gap at the $\bar{\Gamma}$ point. These states are further illustrated in Fig. 2(e1–e3), showing data measured at Ge concentrations between 47% and 60% using s-polarization of laser radiation in the vicinity of the initial DP at the $\bar{\Gamma}$ point. Notably, no visible gap is observed in these dispersions for this range of Ge concentrations. This suggests that at these Ge concentrations, the bulk states with the apparent zero gap at the $\bar{\Gamma}$ point are formed within the states with a peak energy splitting of about 100 meV (see corresponding EDCs in Fig. 2(c1–c7)). These data also confirm the existence of a plateau with a zero band gap depending on the Ge concentration, which may be indicative of the formation of a Weyl metal state. The potential formation of this state in $Mn_{1-x}Ge_xBi_2Te_4$ will be analyzed in more detail through theoretical calculations.

At the same time, in addition to the states with an apparent zero energy band gap inside the states with an energy splitting of about 100 meV, pronounced the Ge-contributed Rashba-like states are also observed in the measured dispersions. These Rashba-like states, as depicted in Fig. 1 and Fig. 2, shift towards higher binding energies with increasing Ge concentrations, presumably hybridizing with the states from the upper CB cone in the region of the $\bar{\Gamma}$-point. This hybridization leads to the formation of peaks in the EDC profiles with a visible energy splitting of about 100 meV. For mearurements with He-lamp this state splitting is of about 70 meV. Within the energy region between these states (peaks), as already noted, a non-zero density of electronic states is observed, resulting in the formation of an apparent zero band gap at the $\bar{\Gamma}$-point.

Results of Theoretical Calculations

AFM TI $Mn_{1-x}Ge_xBi_2Te_4$. Calculations of Surface States

Fig. 3(a1–a6) presents the results of electronic structure calculations for a 12 septuple layer (SL) thick $Mn_{1-x}Ge_xBi_2Te_4$ slab with Ge concentrations varying from 0% to 75%. Electronic states with more than 15% localization in the first SL are considered surface states (both topological and trivial ones), highlighted in brown (Figs. 3(a1-a6)), while contributions from atoms in the 3rd, 4th, and 5th SLs are classified as bulk states, represented using a color scale from black through blue to white, where the color reflects the degree of localization in these SLs. Horizontal dashed lines illustrate the energy splitting at the $\bar{\Gamma}$ point between TrSS. Figs. 3(b1–b6) and (c1–c6) represent the corresponding contributions of bulk and surface states (as classified above) to the electronic structure of systems with varying Ge concentration, using a Lorentzian broadening of 30 meV FWHM to simulate ARPES data. The magnitude of the contributions is reflected by the color scale from blue through red to yellow. The red lines in Figs. 3(a1–a3) and (c1–c3) indicate the position of the topological surface states (TSS) in the surface electronic structures, which are highlighted for clarity. White curves in the center of each image depict EDCs of bulk and surface states taken at the $\bar{\Gamma}$ point for comparison with experimental EDCs. Horizontal dashed lines in bulk EDCs indicate the peak positions, while in surface EDCs, they indicate TrSS peak positions. Solid horizontal red lines in surface EDCs indicate the TSS peak position in surface band structures and corresponding energy gap.

Panel (a) shows that the energy splitting between VB and CB (the branches of blue color) decreases as Ge concentration increases. The gap in TSSs at the Dirac point at low Ge concentrations decreases to nearly zero at $x = 33\%$. At 50% Ge concentration, the TSSs disappear from the spectra, and instead, bulk band states (see blue lines) appear in the region of the initial Dirac point, resulting in a zero gap. Further increases in Ge concentration lead to a reopening of the band gap formed by bulk states, with a slight decrease at $x = 75\%$. Nonetheless, TrSS, shown in light brown near the edges of the CB and VB, also contribute to the band dispersion. These states shift towards DP as Ge concentration increases. Rashba-like surface states, which are discernible in the band dispersions, shift towards higher energies with increasing Ge concentration. Beyond 50% concentration, hybridization between Rashba-like states and CB states becomes pronounced, resulting in characteristic Rashba-like structure with small cone at the $\bar{\Gamma}$-point with the gap formed by TrSS.

Simulated ARPES data in panel (b) demonstrate that even in bulk-sensitive signals, the distance between the most intense EDC peaks differs from the actual energy splitting between the VB and CB. Thus, we do not observe the closure of the gap by bulk states at 50% due to the low density of bulk states near the Fermi level. Additionally, such a simulation poorly describes the behavior of the gap observed in the experimental dispersions shown in Figs. 1 and 2. This inconsistency can be attributed to surface sensitivity in experimental measurements.

In the case of surface-sensitive simulated ARPES data in panel (c), surface states significantly contribute to the signal, and therefore the behavior of the distance between the most intense EDC peaks closely follows the energy splitting between them in panel (a). With the chosen broadening of photoemission lines, the gap in TSS becomes visually indistinguishable at $x = 25\%$ (the Dirac cone states positions highlighted by horizontal red lines). At the same time, at all concentrations, peaks related to TrSS and the energy distance between them are clearly discernible, which is quite close to the energy interval separating these states in panel (a). As the Ge concentration increases, a gradual decrease in the distance between these peaks, followed by a slight increase at $x = 75\%$, can be observed. Notably, in the case of nearly zero or zero gap at $x = 25\%$ and $x = 50\%$, due to the presence of TrSS peaks, the gap estimation from such EDC will yield a non-zero value, the so-called apparent band gap.

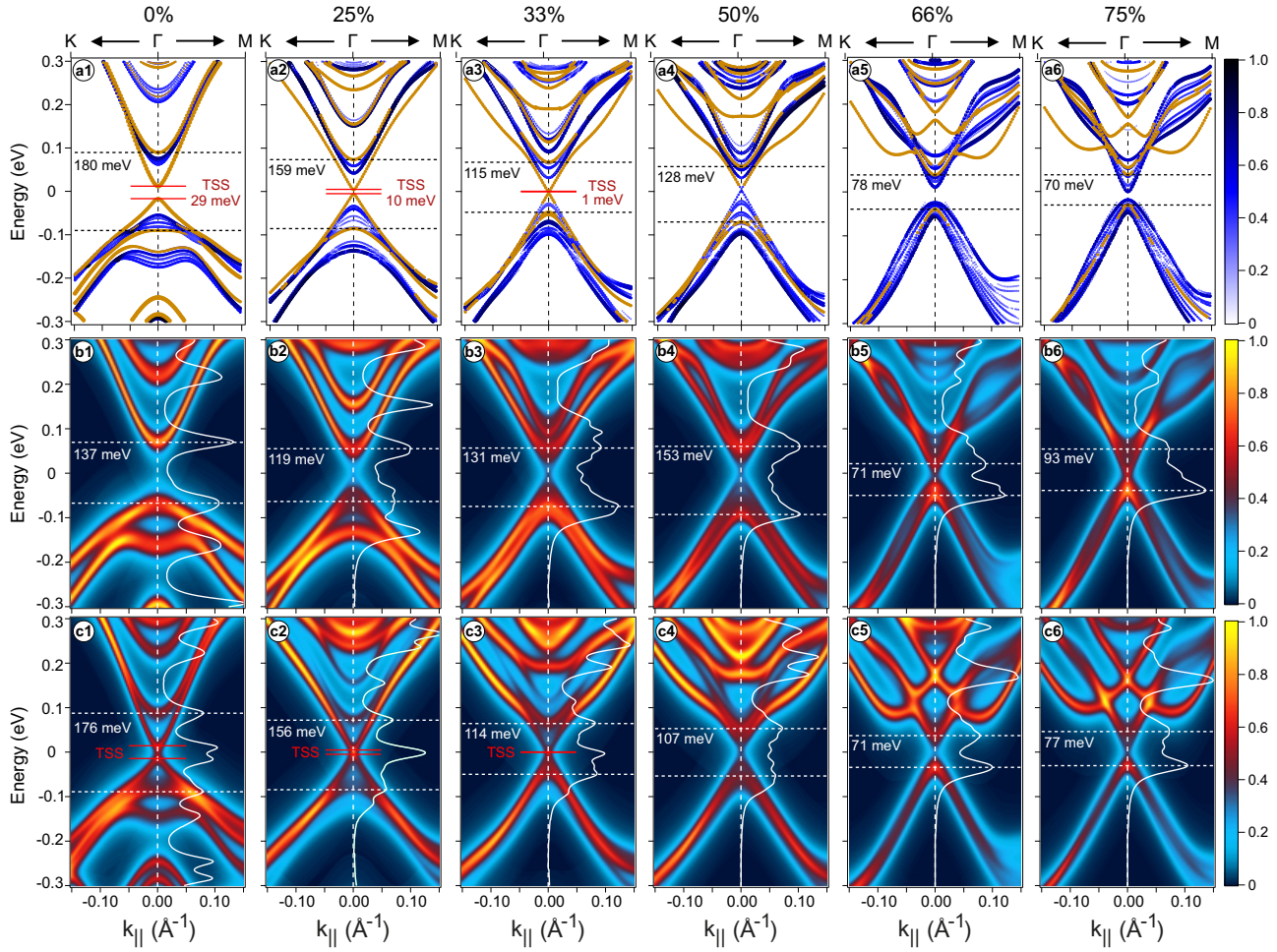

Figure 3. (**a1**–**a6**) Calculated band structure of a 12 SL thick slab of $Mn_{1-x}Ge_xBi_2Te_4$ in the *KΓM* direction in the BZ for Ge concentrations from 0% to 75%. Surface states are highlighted in light brown, and bulk states in black-blue-white. Horizontal dashed black lines indicate the energy positions of TrSS at the $\bar{\Gamma}$ point. Horizontal solid red lines indicate the TSS positions, which are present for Ge concentrations up to 33%. (**b1**–**b6**) and (**c1**–**c6**) depict the bulk and surface band structures, respectively, using a Lorentzian smearing of 30 meV FWHM. Each image contains EDCs taken at the $\bar{\Gamma}$ point (white curves). Horizontal white lines indicate the energy positions of EDC peak centers, while solid red horizontal lines show the TSS positions from Figs. (a1–a6).

Thus, simulated ARPES data in panel (b) suggest that estimating the band gap based on EDC peaks may overestimate it due to surface sensitivity in experimental measurements. Panel (c), accounting for surface states, provides a better description,

aligning more closely with experimental findings. Panels (a) and (c) show that, in addition to the TSSs, trivial surface states form on the system's surface, contributing to the dispersion characteristics specific to $Mn_{1-x}Ge_xBi_2Te_4$. These states determine the formation of peaks with energy splittings of 100 and 70 meV, observed in the experimental dispersions in Figs. 1 and 2. The non-zero density of states within the energy state splitting (formed by TrSS) of approximately 70 and 100 meV at Ge concentrations of 45–60% in the experimental spectra suggests the formation of an apparent zero energy gap in theoretical calculations within the concentration range of 33–50%.

Thus, both experimental studies and theoretical calculations of changes in the electronic structure of $Mn_{1-x}Ge_xBi_2Te_4$ confirm the presence of a plateau with a zero bulk band gap as the Ge concentration increases, suggesting the potential formation of a Weyl semimetal state in this system. In the following sections, we will analyze in more detail the possibilities and conditions for the formation of the Weyl semimetal state by examining changes in the bulk electronic structure with variations in the SOC strength and interplanar distances in a system with FM and AFM ordering.

AFM TI $Mn_{1-x}Ge_xBi_2Te_4$: Calculations of Bulk Band Structure

The bulk band structure calculations in the $K\Gamma Z$ direction of the BZ were conducted to explore the possibilities of TPTs in the $Mn_{1-x}Ge_xBi_2Te_4$ system. This direction is important because the $GeBi_2Te_4$ system (100% substitution) exhibits band inversion at the Z point, whereas the $MnBi_2Te_4$ system has its DP at Γ point of the BZ. In our study, TPTs are investigated using Te–Bi p_z band diagrams, where each point is colored red (blue) if the contribution of Te p_z orbitals is greater (lesser) than that of Bi p_z orbitals. These diagrams are used to detect whether band inversions occur at specific points in the Brillouin zone.

Fig. 4(a1–a6) shows the results of bulk band structure calculations of $Mn_{1-x}Ge_xBi_2Te_4$ for $x = 0$, 25%, 33%, 50%, 66%, and 75% along the $K\Gamma Z$ direction. The bulk band gap, highlighted with horizontal dashed lines, diminishes with increasing Ge concentration. The Bi p_z orbital contribution (blue points) dominates at the top of VB near the Γ point for concentrations up to 33%, where the band gap reaches a value of 6 meV. This band ordering corresponds to that of $MnBi_2Te_4$, indicating that the system is in the TI phase. Additional calculations for a Ge concentration of 40% (Fig. 1S Suppl. Inform.) show a band gap value of 9 meV, where Bi p_z still dominates at the top of VB.

Further increase in Ge content to 50% leads to a band inversion within a small region around the Γ point, while the bulk gap is almost zero. The band ordering, where the VB is dominated by Te p_z orbitals everywhere and the Bi p_z contribution dominates a small region of VB around the DP, is characteristic of a trivial insulating phase[20,54]. This suggests that the TPT into a trivial state may occur at some concentration x_0 slightly lower than 50%. This "trivial" band ordering persists at concentrations of 60% and 66% (Fig. 1S). The bulk band gap behaves similarly to the corresponding slab calculations in Fig. 3 when the Ge concentration is further increased: it increases slightly up to 32 meV, but then decreases down to 5 meV at $x = 75\%$.

According to Fig. 1S Suppl. Inform., at a concentration of 80%, the bulk band structure resembles that of the $GeBi_2Te_4$ state. However, the band analysis is hindered by the fact that the unit cell of $GeBi_2Te_4$ is noticeably different from that of $MnBi_2Te_4$ from a geometric standpoint; for example, the cell vector length is different[37].

Fig. 4(b1–b6) illustrates the bulk-projected (along ΓZ) band structure in the KTM direction, allowing for a more direct comparison with the experimental data. The resulting EDC profiles at the Γ point are indicated by red lines.

It should be noted that similar calculations with varying Ge content in $Mn_{1-x}Ge_xBi_2Te_4$ were provided in ref.[37]. In that work, it was shown that supercell calculations with impurities yield results similar to those obtained using a coherent potential approximation (CPA) approach, which is considered to be a more accurate method for dealing with disorder in alloy systems.

Investigation of Possible TPTs and Formation of WSM state in $Mn_{1-x}Ge_xBi_2Te_4$: Model Calculations and Analysis

While the formation of a plateau with a minimum energy gap in the extended concentration range of 30–50% is evident, the underlying physical processes responsible for these observed changes in the electronic structure remain to be investigated. One potential explanation, as suggested in previous studies[35,36,38], is a possible transition to a WSM state within the region of the minimum energy gap. In this study, we aim to conduct a detailed analysis of the potential transition to such a state in $Mn_{1-x}Ge_xBi_2Te_4$ and to identify the factors influencing the occurrence of various TPTs within this system, including the transition from the antiferromagnetic TI state to the WSM state.

It is worth noting that analyzing the possibility of forming magnetic Weyl semimetals and understanding their electronic structure features presents a significant and challenging scientific endeavor, given the unique properties of these materials[43,45,46] and the limited depth of previous studies in the literature. Below, we will present comparative model calculations detailing the changes in the electronic structure for the TI $Mn_{1-x}Ge_xBi_2Te_4$, encompassing both the AFM and FM phases, wherein states characteristic of the WSM can be explicitly discerned[12,13,32–34,44,48]. Additionally, we will conduct model calculations to explore the changes in electronic structure and the corresponding TPTs possible in these systems, accounting for wide variations in the effective value of the SOC and interplanar distances. These variations arise from the gradual replacement of magnetic Mn atoms with non-magnetic Ge atoms.

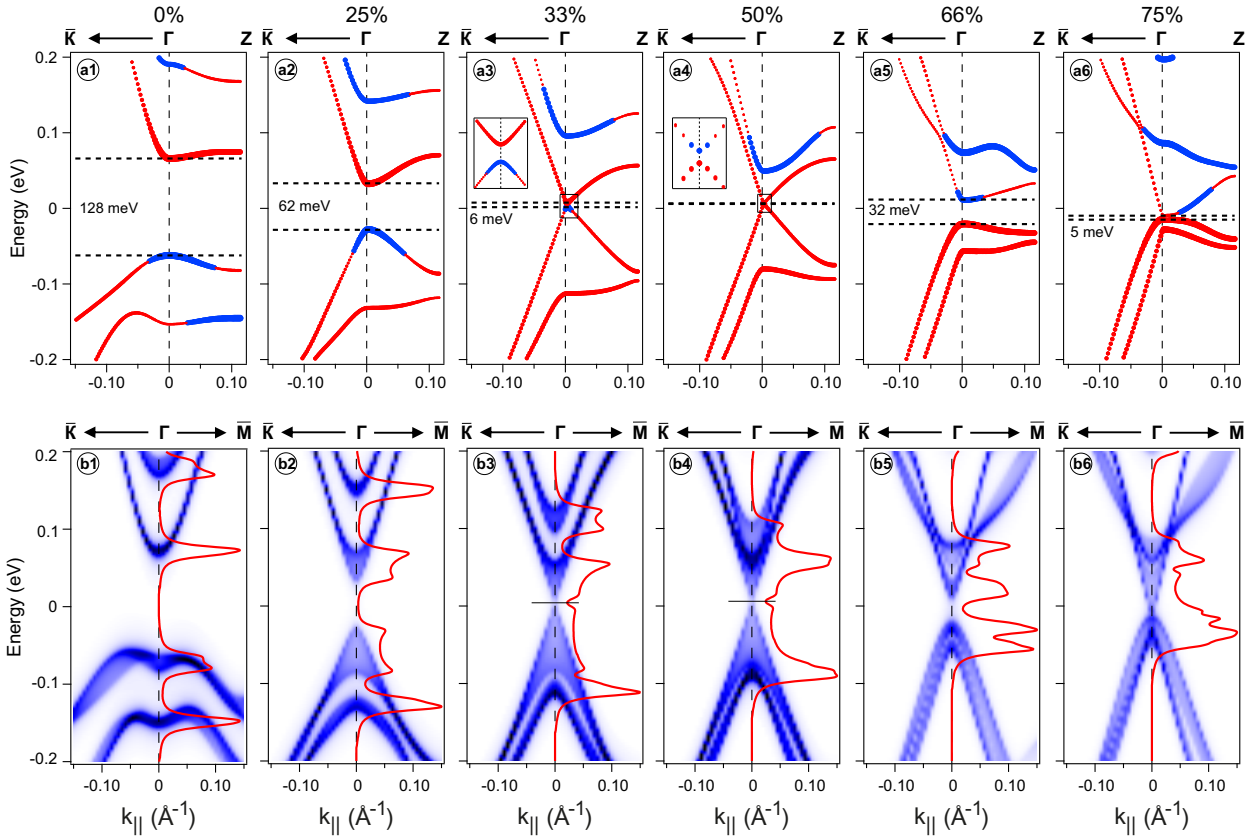

Figure 4. (**a1**–**a6**) Bulk band structure calculations of the $Mn_{1-x}Ge_xBi_2Te_4$ primitive cell in the $K\Gamma Z$ direction for different Ge concentrations up to 75%. Blue (red) points indicate that the Bi p_z orbital contribution at that point is greater (lesser) than the corresponding Te p_z contribution. (**b1**–**b6**) Bulk-projected band structures along the $K\Gamma M$ direction (projection is along ΓZ) for the same Ge concentrations. The EDC profiles at the Γ point are shown as red curves.

Henceforth, we will employ the term "WSM state." Despite the band bending at the surface of the system, under certain conditions, compensation occurs, situating the formed Weyl points near the Fermi level, similar to a typical WSM. Notably, for theoretical calculations that do not consider this band bending, the Weyl points are already situated near the Fermi level, i.e., within the region of zero energy values. To elucidate the factors leading to the formation of a magnetic WSM state, we will meticulously analyze and compare the changes in electronic structure in the ΓZ direction of the Brillouin zone. This direction is pivotal as it corresponds to the region where, according to prior studies[12,13,32–34,44,48], a transition to the magnetic WSM phase should occur in $MnBi_2Te_4$-based systems.

Simultaneously, we postulate that at concentrations of Ge atoms ranging from 40% to 60%, characterized by a zero-like band gap, local violations of the AFM order begin to emerge, or local ferrimagnetic inclusions form. These phenomena can potentially catalyze the formation of the WSM state. At these concentrations, the energy gap at the Γ-point closely approximates the minimum, and the system may exhibit electronic structure features indicative of the transition to this state.

FM $Mn_{1-x}Ge_xBi_2Te_4$: Dependence on the Concentration of Ge Atoms

It is worth highlighting that one of the defining characteristics of the transition to the WSM state[43–46,48,55–57] is the intersection of states with different parities from the VB and CB without the emergence of an energy gap at these state intersections. Concurrently, the transition from AFM TI to the trivial state suggests a possible transition marked by avoided-crossing effects and the formation of a band gap at the intersection point (for comparison, see[20,54]).

In studies investigating the formation of Weyl semimetals and the intricacies of their electronic structure, as well as the conditions conducive to the transition to the WSM state[32–34,43,45,46,48,55–57], it has been demonstrated that such a transition may be triggered by the violation of one of two symmetries: spatial symmetry or time-reversal symmetry, which may arise during the transition from AFM to FM. Furthermore, within the category of ferromagnetic Weyl semimetals (e.g., $MnBi_2Te_4$,

$MnSb_2Te_4$, $MnBi_2Se_4$[32–34,48,57]), it is precisely the violation of time-reversal symmetry and the establishment of FM ordering that dictate the feasibility of transitioning to the WSM state, characterized by state intersections devoid of any energy gap formation.

Simultaneously, in studies such as[6,12,13,44,48], which focus on a comparative analysis of the electronic structure of magnetic TIs directly from the $MnBi_2Te_4$ family in the FM phase (where time-reversal symmetry is violated), it has been demonstrated that the transition to the WSM state (similarly observed in other Weyl semimetals[32–34,43,55–57]) occurs through the intersection of electronic states with different parities in the ΓZ direction of the BZ. In this scenario, two Weyl points (nodes) emerge in the dispersion curves along the $Z\Gamma Z$ direction (symmetrically positioned relative to the Γ-point), i.e., perpendicular to the surface plane of the samples under examination.

Regrettably, these points cannot be directly measured via dispersions taken along the surface; however, they may manifest in such measurements through, for instance, modulation of the gap at the DP and the density of projected bulk states. In light of the foregoing, to validate this hypothesis, this study conducted comparative calculations of the electronic structure (dispersion dependencies) for the FM phase of $Mn_{1-x}Ge_xBi_2Te_4$—systems exhibiting FM ordering—under the gradual replacement of Mn atoms by Ge atoms across a wide range of substitution concentrations.

Fig. 5(a1–a7) presents the results of bulk electronic structure calculations for FM $Mn_{1-x}Ge_xBi_2Te_4$ at Ge concentrations of 0, 16, 25, 33, 50, 66, and 75%. Notably, these calculations reveal that for the FM phase of TI $Mn_{1-x}Ge_xBi_2Te_4$ with Ge concentrations ranging from 0% to 50%, the intersection of VB and CB states characteristic of a WSM is indeed observed in the ΓZ direction of the BZ, consistent with previous findings[6,12,13,32–34,43,44,48,55–57]. This intersection occurs at the Weyl point located at $k_{||} = 0.015 - 0.02\text{Å}^{-1}$ (it is marked as WP), with a similar Weyl point characterized by opposite chirality observed in the opposite direction ($-\Gamma Z$), as expected for magnetic Weyl semimetals with time-reversal symmetry violation.

Additionally, within the concentration range up to 50% (particularly notable within the 33-50% range), a minor energy gap of approximately 10 meV is present at the Γ-point, exhibiting minimal variation within this concentration range. Conversely, for Ge concentrations of 66% or higher, the absence of state intersections in the ΓZ direction of the BZ results in the formation of a band gap across the entire BZ, indicating a transition of the system to a presumably trivial insulator state. In the presented dispersions, the contributions of Te p_z and Bi p_z states are depicted in red and blue, respectively.

Analysis of the changes in contributions reveals that for the FM phase of $Mn_{1-x}Ge_xBi_2Te_4$, the contribution of Te p_z states predominates in the region of the formed Weyl points, with no discernible inversion of contributions from Te p_z and Bi p_z states observed for Ge concentrations up to 50%. It is worth noting that the WSM state is also topological[43,45,46]. A similar trend in the contributions of Te p_z and Bi p_z states at the edges of branches at the Γ-point in the vicinity of the Weyl point was also documented in[32] for the FM phase of $MnBi_2Se_4$ during the transition to the WSM state.

With further increases in Ge concentration up to 66%, a distinct inversion of contributions from Te p_z and Bi p_z states at the edges of the newly formed energy gap at the Γ-point becomes apparent. In this scenario, the sequence of prevailing contributions from Te p_z and Bi p_z states at the edges of the gap more closely resembles that characteristic of a trivial insulator.

In general, the reduction in Mn atom concentration (via their replacement with non-magnetic Ge atoms) in the FM phase leads to a gradual decrease in the splitting between state branches at the Γ-point and a shift of Weyl points towards the Γ-point. Between Ge concentrations of 50 and 66%, the Weyl points annihilate at the Γ-point, transitioning the system from a WSM to a trivial insulator state. Fig. 5(b1–b7) illustrates the dispersions of bulk states projected from the ΓZ direction of the BZ onto the $K\Gamma Z$ direction. The red lines depict corresponding EDC profiles taken directly at the Γ-point (for comparison with experiment and calculations for the AFM phase).

A key distinction between these calculations and those for the AFM phase (shown in Fig. 4) is the presence of a peak in the EDCs in the energy region of the intersection of branches at the Weyl point. This peak arises from the contribution of states projected from the ΓZ direction and their intersection in this direction, serving as an indicator of the realization of the WSM state with a zero band gap in the vicinity of the Weyl point. It is marked by horizintal stripe. This peak in the EDCs at the Γ-point remains evident up to Ge concentrations of 50%. Conversely, for the AFM phase in the region of the DP, a dip in the EDCs was observed.

At a concentration of 66%, coinciding with the transition to the trivial insulator state, this peak is supplanted by an energy gap at the DP in both the $K\Gamma Z$ dispersions and corresponding dispersions of bulk projected states in the $K\Gamma M$ directions. Additionally, other peaks in the EDCs, situated further in energy from the Dirac and Weyl points, shift towards the DP with increasing Ge concentration, mirroring experimental observations and theoretical calculations for the AFM phase.

Interestingly, for a Ge concentration of 50%, the energy gap between these bulk state peaks correlates even more closely with the experiment than for the AFM phase. Moreover, if we directly compare the EDC at the Γ-point for the AFM (see Fig. 4(b4)) and FM phase (see Fig 5(b5)) at the Ge concentrations in the region of 50% with the experimental EDC profile in Fig. 2(c4,c5), then the experimental profiles (with the presence of some peak at the initial DP instead of a dip) are more likely to correlate precisely with calculations for the FM phase with this Ge concentration.

This may be an additional argument in favor of the possibility of a transition to the FM phase (or ferrimagnetic phase)

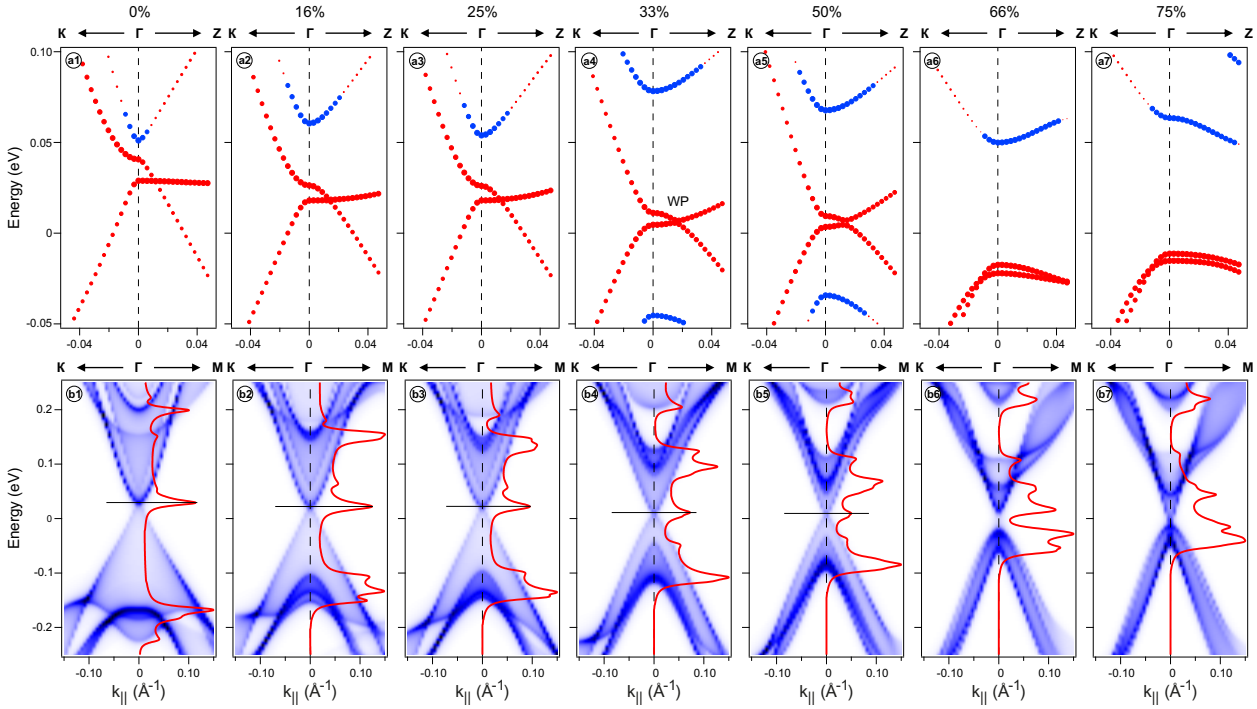

Figure 5. (**a1**–**a7**) Theoretically calculated changes in the dispersion dependencies of bulk states in the *KΓZ* direction of the BZ for FM TI $Mn_{1-x}Ge_xBi_2Te_4$ with varying Ge concentration from 0 to 75%. Changes in the contributions of the Te p_z and Bi p_z states are shown in red and blue, respectively. (**b1**–**b6**) Theoretically calculated dispersion dependencies of the projected bulk states from the *ΓZ* direction to the *KΓM* directions of the BZ. The profiles of the density of electronic states at the Γ-point are shown by red lines, depending on the concentration of Ge atoms.

and the formation of the WSM state in the real $Mn_{1-x}Ge_xBi_2Te_4$ system at the Ge concentrations of 40–55%, at least for the forming local FM inclusions (see Fig. 9). Now the question arises: how can a transition from the AFM TI phase to the WSM phase actually occur under partial replacement of atoms of magnetic metals (Mn) with atoms of a non-magnetic element (Ge) and under what conditions? If we assume that in the region of Ge concentrations of 45–55% with a minimum (zero-like) band gap, some features of such a transition manifest themselves in experimental spectra, then this phase transition is plausible.

As previously noted, the WSM phase for compounds from the $MnBi_2Te_4$ family (with the replacement, complete or partial, of Te atoms by Se atoms or Bi atoms by Sb atoms, etc.) can be realized primarily with the FM type of interactions[6,32–34,44,48,57,58]. It should be noted here that the probability of the implementation of the FM phase in the family of TIs based on $MnBi_2Te_4$ can be greatly influenced by the formation of antisite substitution defects of the Mn/Bi type, when Mn atoms are located at the sites of Bi atoms in the space between the magnetic layers (and vice versa), thereby modulating the exchange interaction between magnetic Mn layers[19,34,58,59].

This leads to modulation of the magnetic interaction between the nearest magnetic layers due to a change in the effective SOC strength since interaction between magnetic layers occurs through Mn–(Bi, Te)–Mn superexchange between magnetic layers through non-magnetic Bi, Te layers. The introduction of Mn atoms in place of Bi atoms can lead to the formation of ensembles of Mn atoms with AFM (opposite) spin orientation relative to the original Mn layers, which can locally (in the region of Mn localization at Bi sites) change the type of magnetic interaction from AFM to FM, as observed in systems based on $MnSb_2Te_4$, where the formation of antisite substitution defects of the Mn/Sb type is actually observed[48,58–60].

Moreover, in systems with partial replacement of Mn atoms by Ge atoms ($Mn_{1-x}Ge_xBi_2Te_4$), the formation of the above-mentioned substitution defects of the Mn/Bi type also increases, which increases the probability of transition to the FM phase with the growth of concentration of Ge atoms, thereby creating conditions for the transition to the WSM state. On the other hand, because the interaction between Mn atoms in $MnBi_2Te_4$ occurs by superexchange through Te and Bi atoms, the replacement of Bi atoms with Ge atoms will also modulate the exchange interaction between Mn atoms, both within the layer and between the neighboring Mn layers, stimulating the corresponding transition from AFM to the FM state, taking into account that the formation energies of the AFM and FM phases are practically comparable for Ge concentrations from 30 to 60%.

The transition from AFM TI to FM TI, which takes place in the $(MnBi_2Te_4)_n(Bi_2Te_3)_m$ family during the transition to $MnBi_6Te_{10}$ compounds and further to $MnBi_8Te_{13}$ (see, for instance,[22,23]) can also be considered as modulation of the exchange interaction between magnetic Mn layers through non-magnetic Bi_2Te_3 blocks.

Changes in Electronic Structure Upon Modulation of SOC Strength for FM and AFM $Mn_{1-x}Ge_xBi_2Te_4$

To test the assumption regarding the influence of variations in the SOC strength on the modulation of Mn–(Bi, Te)–Mn superexchange, and consequently, on the change in the magnetic interlayer Mn–Mn interaction, which determines the possible transition between the phases of TI and WSM, as well as a trivial insulator, model calculations were conducted. The influence of SOC strength modulation was examined for the $Mn_{1-x}Ge_xBi_2Te_4$ system with an initial Ge concentration of 50% in both the AFM and FM phases for comparison. It is presumed that for a system with 50% Ge substitution, where the band gap is at its minimum, the transition to the WSM phase in a real system is most probable.

Fig. 6(a1–a9) illustrates the theoretically calculated changes in the dispersion dependencies for the $Mn_{1-x}Ge_xBi_2Te_4$ system with $x = 0.5$ and FM-type ordering (FM phase) in the $K\Gamma Z$ direction in the BZ, while varying the SOC strength λ_{SOC} relative to the initial value of 1 (corresponding to a Ge concentration of 50%). Additionally, the corresponding changes in the contributions of the Te p_z and Bi p_z states are depicted in red and blue.

The analysis of these calculations reveals a clear visibility of the intersection of state branches in the ΓZ direction at the Weyl point (at $\lambda_{SOC} = 1$), as well as a change in its position along the ΓZ direction with variations in SOC strength. A similar Weyl point is located inversely relative to the Γ-point in the $-\Gamma Z$ direction.

The calculations indicate that a decrease in SOC strength (corresponding to further Mn atom replacement with Ge atoms for Ge concentrations exceeding 50%) results in a shift of the Weyl point in the ΓZ direction towards the Γ-point (and the second point on the opposite side $-\Gamma Z$). This shift leads to the annihilation of these two Weyl points (at $\lambda_{SOC} = 0.94$) and a transition from the WSM structure to the Dirac semimetal structure with the DP at the Γ-point. Subsequently, with further decreases in SOC strength, an absolute gap forms at the Γ-point, which enlarges as the SOC strength diminishes.

The inversion of the contributions of the Te p_z and Bi p_z states at the gap edges, relative to those observed for AFM TI (see Fig. 4(a1)), suggests that a transition to the trivial insulator phase occurs as the SOC strength decreases.

With an increase in the SOC strength relative to $\lambda_{SOC} = 1$, corresponding to a decrease in the Ge concentration below 50%, the Weyl point (and its inverse in the $-\Gamma Z$ direction) also shifts towards the Γ-point. At $\lambda_{SOC} = 1.08$, two Weyl points also annihilate at the Γ-point, resulting in the formation of the Dirac semimetal state with a single intersection point at the Γ-point. Further increase in the SOC strength leads to the reopening of the band gap at the Γ-point, inducing a TPT to the TI phase. In this state, the contributions of the Te p_z and Bi p_z states at the gap edges follow the same sequence as for AFM TI (Fig. 4(a1)), albeit in this case, it is a FM TI. This transition from the WSM state to the TI state with increasing SOC strength is unexpected yet promising.

Thus, the SOC strength can alter the effective exchange interaction in the system, leading to a series of TPTs between phases of magnetic topological or trivial insulators, through phases of Dirac, Weyl, and again Dirac semimetals, depending on the increase or decrease in the SOC strength. For comparison, Fig. 6(b1–b6) illustrates model calculations of changes in dispersion dependencies in the $K\Gamma Z$ direction of the BZ and corresponding changes in the band gap size when modulating the SOC strength, relative to a system with a Ge concentration of 50%, but with AFM interactions. The corresponding changes in the contributions of the Te p_z and Bi p_z states are also shown.

The initial state (at $\lambda_{SOC} = 1$) features a zero-like band gap in the region of zero energies (at the DP), closely resembling a Dirac semimetal state. As the SOC strength decreases, the gap opens at the DP, increasing with decreasing λ_{SOC}. The inversion of the contributions of the Te p_z and Bi p_z states at the gap edges relative to the sequence characteristic of AFM TIs indicates a TPT to the trivial insulator phase. Conversely, with an increase in λ_{SOC} relative to $\lambda_{SOC} = 1$, the gap at the DP reopens, with a sequence of contributions from Te p_z and Bi p_z states at the gap edges characteristic of AFM TI. This implies that an increase in the SOC strength leads to a transition to the AFM TI phase, occurring within a very narrow range of changes in the SOC strength.

As a result, these calculations reveal that in the AFM phase, obtaining a plateau in the minimal band gap size dependence with variations in the SOC strength is impossible. Moreover, for the AFM phase, intersections of states in the ΓZ direction of the BZ are not observed, indicating that the transition to the Weyl metal state does not occur in this phase. This transition is only possible for a system in the FM state or upon transition to the FM (or ferrimagnetic) state.

Schematically, the transition through the WSM state for the FM phase and its absence for the AFM phase can be represented by the diagram shown in Fig. 7. This diagram demonstrates the relationship between the modulation of the SOC strength, the presence of an exchange field (breaking the time-reversal symmetry), and the resulting change in the formed energy gap. For AFM phases (Fig. 7 (a)), changes in the gap on the SOC strength are described by the dependence characteristic of TPT from the state of a topological insulator to the state of a trivial insulator (see blue arrows in Fig. 7 (a)) with a minimum (ideally zero) gap at the TPT point, as in Fig. 6(b).

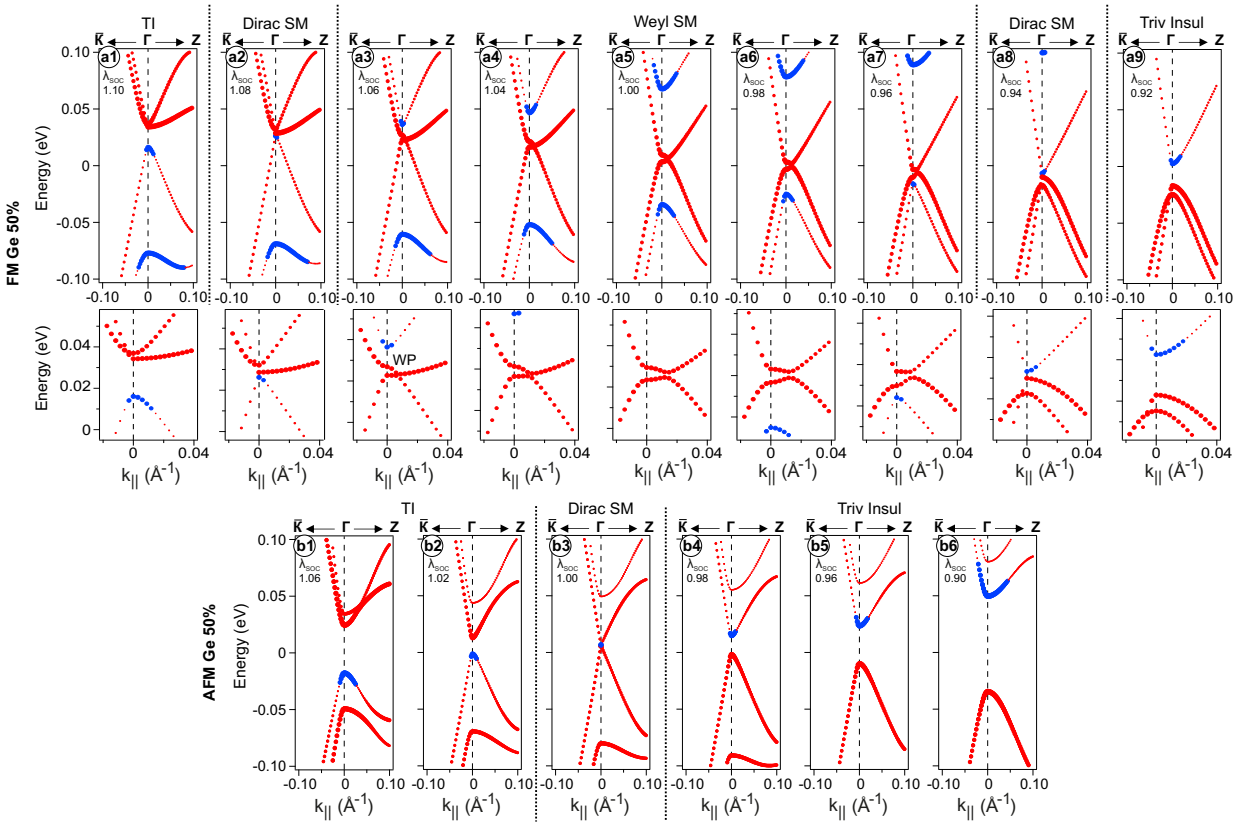

Figure 6. Theoretically calculated changes in the dispersion dependencies of bulk states for the FM (**a1**–**a9**) and AFM (**c1**–**c6**) phases of $Mn_{1-x}Ge_xBi_2Te_4$ with $x = 0.5$ in the $K\Gamma Z$ direction of the BZ. The modulation of the SOC strength λ_{SOC} on the Te and Bi atoms is relative to the initial value, taken as 1. Changes in the contributions of the Te p_z and Bi p_z states are shown in red and blue, respectively. (**b1**–**b9**) Detailed representation of dispersion dependencies in the region of the intersection of branches of states in the ΓZ direction of the BZ for the FM phase and the corresponding shift of the Weyl point with changing SOC strength.

The availability in the system of an exchange field (uniform or local one), which violates the time-reversal symmetry, leads to the fact that the contributions to the gap formation due to the influence of the SOC and exchange interaction contributions are compensated at a certain strength of the SOC strength. As a result, the point of the zero value of the gap (DSM state) on the dependence of the gap on the SOC strength transforms into a line, which corresponds to the WSM phase (but edges of this line still represent DSM states, see red lines in Fig. 7 (b)). In this region, TPT occurs from the topological to the trivial state and vice versa through the intermediate phase of the WSM.

As the exchange field decreases, the region of realization of the WSM state also decreases, shrinking to zero and resulting in the existence of a single point of the DSM phase, as shown in Fig. 7 (a). This representation correlates with the results of works[61–63], showing the necessity for the formation of an intermediate phase of the WSM under the transition from a topological to a trivial state in systems with the violation of time-reversal symmetry (or with the violation of inversion symmetry).

AFM and FM $Mn_{1-x}Ge_xBi_2Te_4$. Influence of Variation of Interplanar Distances

Interestingly, when compared with changes in the electronic structure resulting from variations in interplanar distances for both the AFM and FM phases (analogous to stretching and compression of the crystal lattice, akin to changes in pressure normal to the surface), these alterations exhibit fundamental similarities to those induced by changes in SOC strength.

Fig. 8(a1–a7) and (b1–b7) depict the outcomes of model calculations of electronic structure changes (dispersion dependencies) for the AFM and FM phases of the $Mn_{1-x}Ge_xBi_2Te_4$ system with varying interplanar distances (i.e., compression and tension), relative to the original system with a Ge concentration of 50%. Here, (+) indicates an increase in the interplanar distance, while (−) signifies its decrease. In this context, the Ge50% unit cell underwent compression or stretching by scaling

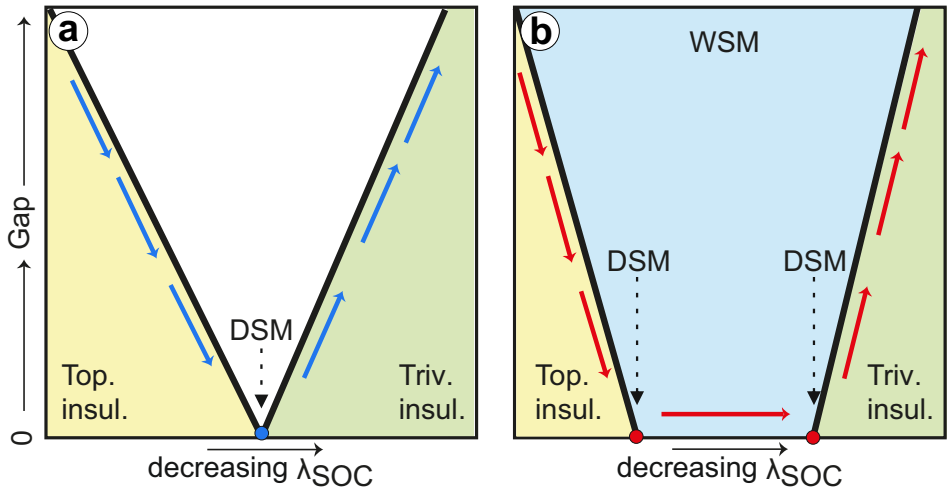

Figure 7. Scheme of TPTs occurring in AFM TI in the absence (**a**) and presence (**b**) of an uncompensated FM component in the system, represented by the dependence of the gap size on the SOC strength. Changes in the system state on the phase diagram are shown by blue and red arrows, as well as circles.

the interplanar distance (or z-coordinate of the atoms) and the lattice c-vector by the corresponding factor, thereby inducing compression/stretching solely along the normal to the surface plane.

From the presented calculations (Fig. 8(a1–a7)), it becomes evident that in the AFM phase, with lattice expansion relative to the initial state ($\gamma c_z > 1$), a TPT to the trivial insulator state occurs. This transition involves a reinversion of contributions from the Te p_z and Bi p_z states at the edges of the gap at the DP relative to the characteristic sequence for TI, mirroring changes observed with decreasing SOC value. Conversely, when the interplanar distance decreases relative to its initial value (i.e., when $\gamma c_z < 1$), transitions to the AFM TI state occur, with a corresponding sequence of contributions from the Te p_z and Bi p_z states at the edges of the resulting gap, reminiscent of TI.

These observed processes closely resemble those occurring during SOC variations, with TPTs featuring a minimum band gap occurring at a single point. Notably, there is no plateau in the behavior of the minimum gap for the AFM phase.

For the **FM phase** (Fig. 8(b1–b7)), the changes in electronic structure exhibit a series of TPTs. In the initial state ($\gamma c_z = 1$) for the FM phase, the system exists as a WSM with intersecting branches of states in the ΓZ direction of the BZ. As interplanar distances expand, the Weyl point gradually shifts towards the Γ-point, and at $\gamma c_z = 1.025$, the Weyl points (nodes) annihilate at the Γ-point. Subsequently, a TPT occurs into a state of trivial insulator. At the Γ-point, there is a reinversion of the contributions of the Te p_z and Bi p_z states at the edges of the energy gap relative to the characteristic sequence of TI, mirroring changes observed with decreasing SOC strength.

Conversely, as the interplanar distance decreases, the Weyl point also shifts towards the Γ-point, and at $\gamma c_z = 0.96$, the Weyl points annihilate at the Γ-point, forming the Dirac semimetal state with a zero energy gap at the DP. Further lattice compression at $\gamma c_z = 0.95$ or less leads to a transition to the TI state, characterized by a corresponding sequence of contributions from the Te p_z and Bi p_z states at the edges of the formed gap, typical of TI. Fig. 8(c1–c7) shows in more detail the changes in electronic structure in the Weyl point region.

Thus, the observed processes closely resemble those occurring under SOC strength variations. Notably, the observed changes suggest the potential formation of a plateau with a minimum energy gap at the Γ point in the dependence of gap size changes with variation of interplanar distances, akin to changes induced by alterations in effective SOC strength values.

It is worth noting that the processes of electronic structure changes in the FM phase, as derived from the calculation results, exhibit a series of TPTs and warrant further theoretical and experimental investigation. Of course, the possibility of transition to the FM phase remains through system remagnetization upon application of an external magnetic field, considering that for $Mn_{1-x}Ge_xBi_2Te_4$ with a Ge concentration of approximately 50%, the magnetic field magnitude required for this remagnetization is significantly less than for pure $MnBi_2Te_4$[42].

Possibility of Transition to the WSM State Directly from the AFM TI Phase

Analyzing the entirety of experimental and theoretical data presented above, we can infer that in the initial stage, as the Ge concentration increases to 30%, the system resides in the AFM TI state. This state is characterized by a reduction in the band gap to minimum values with increasing Ge concentration, as evidenced by the presence of TSSs visible in the experimental

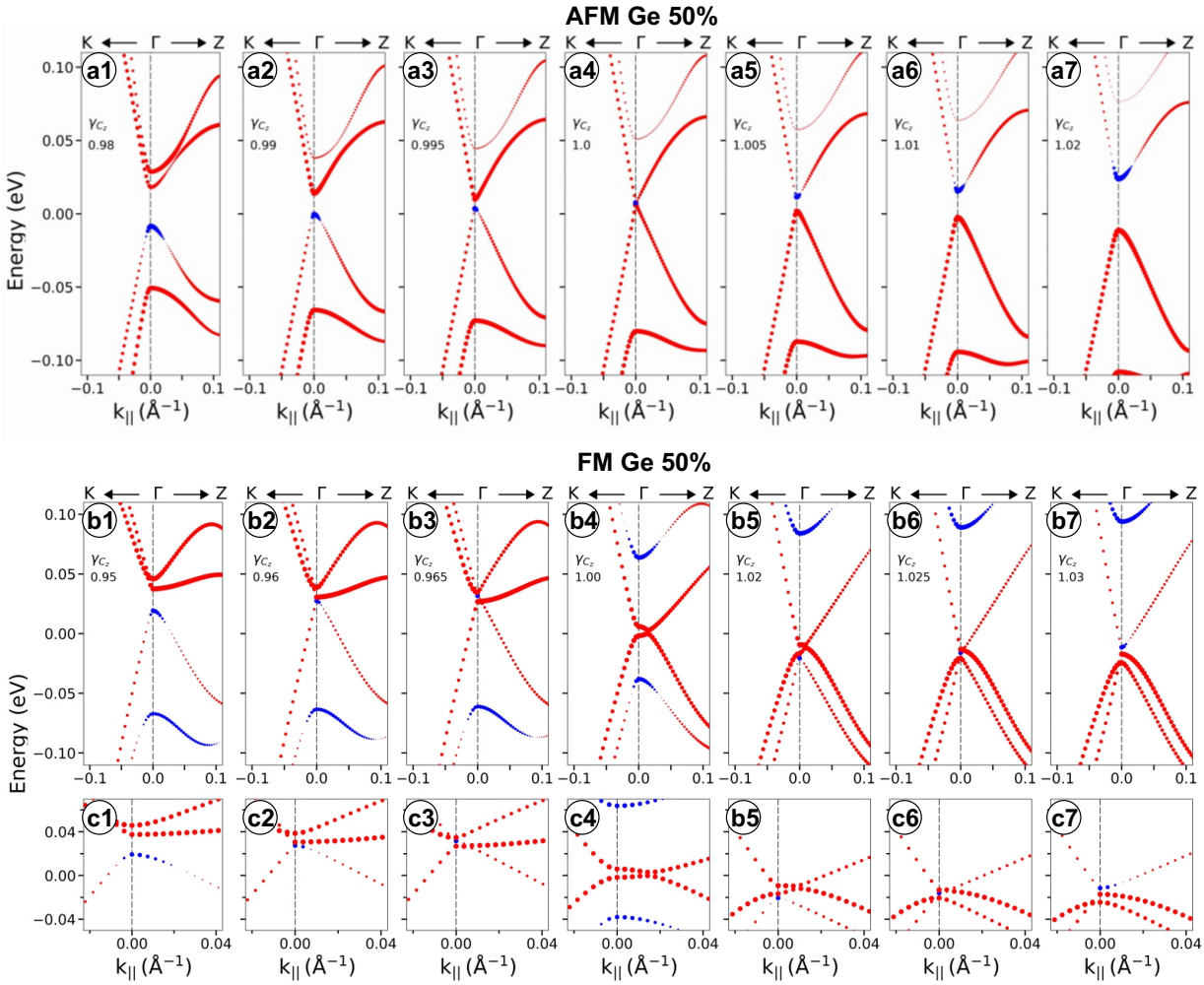

Figure 8. Theoretically calculated changes in the dispersion dependencies of the bulk states in the ΓZ direction of the BZ for $Mn_{1-x}Ge_xBi_2Te_4$ with $x = 0.5$ for AFM - (**a1**–**a7**) and FM - (**b1**–**b7**) phases with variations of compression and tension of the crystal lattice parameter c relative to the initial one, taken as $c = 1$. Changes in the contributions of the Te p_z and Bi p_z states are represented in red and blue, respectively. The insets (c1–c7) show detail in the region of the Weyl point for the FM phase (the intersection of the states in the ΓZ direction).

spectra until the Ge concentration reaches 37%. Theoretical descriptions align well with these observations, depicting changes in electronic structure for AFM TIs within these limits.

As the Ge concentration further increases, states near the DP transform into bulk states, leading to the disappearance of TSSs from the spectra and the emergence of bulk Ge-contributed states around the DP region. Concurrently, the accumulation of antisite defects occurs in the system, facilitating the transition of either the entire system or a portion of it to the FM (or ferrimagnetic) state. This potentially enables local implementation of the WSM state within Ge concentrations ranging from 40% to 50–60%. Moreover, electronic structure alterations, including variations in bulk band gap size, characteristic of the FM phase, are discernible within these concentrations. However, part of the system remains in the AFM state, manifesting corresponding electronic structure changes typical of the AFM phase.

As the Ge concentration exceeds 60–65%, a transition to the trivial insulator phase occurs for both the FM and AFM phases, according to calculation results. Subsequently, with further increases in Ge concentration, a shift occurs towards Mn-doped $GeBi_2Te_4$. Evidence supporting the transition from an AFM TI to a trivial insulator phase with changing Ge concentration possibly occurring through the WSM phase is provided by work[61], demonstrating that the WSM phase serves as an intermediate phase during the transition from TI to trivial insulator states for compounds such as $LaBi_{1-x}Sb_xTe_3$, among others. This transition includes the formation of a plateau exhibiting a zero band gap in the region of such a phase transition.

Additionally, the realization of the critical WSM phase (i.e., the plateau region with zero band gap) can be highly sensitive to the chosen path in the parameter space, suggesting flexibility in engineering the WSM phase. Similarly, in[62], it was shown that the phase diagram of a multilayer structure composed of identical thin films of a magnetically doped 3D topological insulator, separated by ordinary-insulator spacer layers, contains a WSM phase. This phase acts as an intermediate phase between topological and ordinary insulators for systems with broken time-reversal symmetry.

In the case of a system with FM ordering, this transition through the WSM phase occurs naturally due to the breaking of time-reversal symmetry, with the corresponding parameters being changes in SOC strength or interplanar distance in the crystal lattice. Conversely, in the AFM phase, where changes in these parameters are insufficient, additional parameters such as introducing an asymmetric distribution of sites for Mn atom substitution with Ge atoms or the presence of corresponding Bi/Mn antisite defects may facilitate the transition to the WSM phase. Hence, calculations solely involving changes in SOC strength or lattice contraction/expansion for the AFM phase do not demonstrate the formation of the intermediate WSM phase. However, calculations depicting changes in electronic structure with varying Ge concentration do show the presence of a plateau in the band gap minimum characteristic of the WSM.

An additional factor that may stimulate the transition to the WSM phase (at least locally) at certain Ge concentrations is the asymmetry of the local magnetic order when Mn atoms are replaced by Ge atoms. Fig. 9(a1–a4) presents the results of model calculations depicting changes in dispersions for $Mn_{1-x}Ge_xBi_2Te_4$ in the $K\Gamma Z$ direction of the BZ with a change in Ge concentration under the condition of alternating replacement of Mn atoms with Ge, not in each Mn layer, but through the layer (in contrast to disordered placement of Ge atoms).

Model depictions of Ge and Mn atom placement for such a system are also provided in the insets above. This structure bears some resemblance to the multilayer structure composed of a stack of thin layers of magnetically doped 3D TI, separated by insulating spaces studied in[62], where the 3D WSM phase was realized.

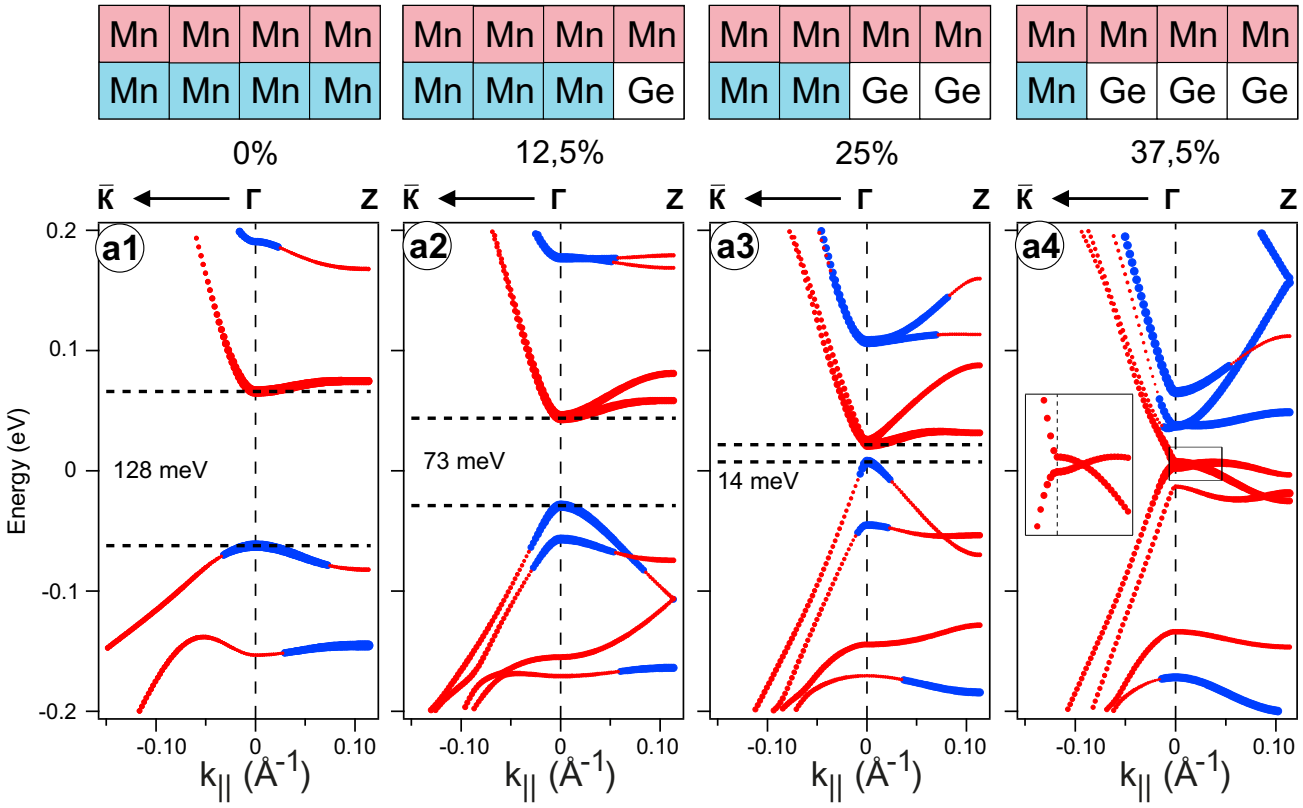

Figure 9. Theoretically calculated changes in the electronic structure of AFM TI $Mn_{1-x}Ge_xBi_2Te_4$ with varying Ge concentration under the condition of alternate replacement of Mn atoms with Ge through the Mn layer. Model depictions of the placement of Ge and Mn atoms are shown in the insets above (red and blue colors denote AFM ordering of Mn layers). For the Ge atom concentration of 38%, a more detailed representation is shown in the region of the intersection of states in the ΓZ direction of the BZ, characteristic of a WSM.

The presented dispersion dependencies reveal a monotonic decrease in the bulk band gap size to 14 meV with an increase in the Ge concentration, consistent with both theoretical and experimental spectra within the concentration range of 0 to 25%. Additionally, some local splitting of the dispersion branches can be observed, possibly associated with an increasing disruption in the AFM interaction.

At a Ge concentration of 38% (Fig. 9(a4)), the intersection of state branches in the ΓZ direction, characteristic of the transition to the WSM state, is observed in the vicinity of the initial DP (zero energies). This results in the formation of corresponding Weyl point(s) in the ΓZ and $-\Gamma Z$ directions, similar to observations in the FM phase. This phenomenon is more clearly illustrated in the inset of Fig. 9(a4).

The splitting between states adjacent to the band gap minimum at this concentration closely aligns with the experimentally observed splitting of corresponding states in Figs.1 and 2. The distribution of Te p_z and Bi p_z contributions to the states at the edges of the bulk gap behaves as expected during the transition from an AFM TI (Figs.4 and 6) to the WSM (Figs. 5 and 6).

These calculations suggest the potential formation of the WSM state in the initial AFM TI $Mn_{1-x}Ge_xBi_2Te_4$ at Ge concentrations ranging from 40% to 55% within the plateau region for the minimum of the bulk band gap. This occurs alongside local violations of the AFM-type interaction, where the replacement of Mn atoms with Ge is not disordered in each Mn layer but occurs through the Mn layer.

Details of DFT Calculations

First-principles calculations in the framework of the density functional theory (DFT) were performed at the Computing Center of SPbU Research park. The electronic structure supercell calculations with impurities were performed using the OpenMX software code, version 3.9.9, which provides a fully relativistic DFT implementation with localized pseudoatomic orbitals[64–66] and norm-conserving pseudopotentials[67]. The exchange correlation energy in the PBE version of the generalized gradient approximation was employed[68].

Impurity concentrations of 25%, 50% and 75% were modeled using the 2×2 supercell, which provides 4 sites for impurity atoms; concentrations of 33% and 66% were obtained using the 3×1 supercell, which allows 3 sites for impurity atoms; impurity concentration of 16% was achieved in the 6×1 supercell, which admits 6 impurity sites.

The surface calculations were performed using 12 SL slabs of $MnBi_2Te_4$ with 20 Å vacuum separation between crystal surfaces. The accuracy of the real-space numerical integration was specified by the cutoff energy of 300 Ry, and the total energy convergence criterion was 10^{-6} Hartree. Uniform reciprocal space meshes for Brillouin zone sampling were specified as $7\times7\times7$ for pristine bulk calculations, $5\times5\times1$ mesh for pristine $MnBi_2Te_4$ slab calculations, and $3\times3\times7$ for bulk and $3\times3\times1$ for slab supercells with impurities, respectively.

All calculations were performed using pseudoatomic basis sets of Bi8.0-s3p2d2f1, Te7.0-s3p2d2f1, Mn6.0-s3p2d1, Ge7.0-s3p2d2, where the pseudopotential cutoff radius is followed by a basis set specification. The Mn $3d$ states were treated within the DFT+U approach[69] using the Dudarev scheme[70] with $U=5.4$ eV. The resulting magnetic moment on Mn atoms in all self-consistent calculations was equal to 5.0 μ_B.

Experiment Details

ARPES measurements (Fig. 1 a1-a8) were performed at the Rzhanov Institute of Semiconductor Physics SB RAS (Novosibirsk, Russia) using the SPECS ProvenX-ARPES facility equipped with the SPECS ASTRAIOS 190 analyser. He Iα ($h\nu=21.2$ eV) radiation was used for these ARPES measurements, and Al Kα ($h\nu=1486.7$ eV) radiation was used for stoichiometry estimation of the samples by means of X-ray photoelectron spectroscopy (XPS).

Laser-based experiments were performed at the μ-Laser ARPES station with Scienta R4000 analyzer (Fig. 2 a1–a4,a7) and LaserSpin ARPES station with Scienta DA30 analyzer (Fig. 2 a5,a6) at HiSOR (Hiroshima, Japan)[52,53]. A laser beam with photon energy of $h\nu=6.3$ eV and a photon flux of up to 10^{14} photons/s was used for the μ-ARPES measurements. The expected energy resolution was approximately 5 meV. The incident photon beam spot diameter was estimated to be 5–10 μm.

During the measurement process, the temperature of the samples was maintained below 30 K. The base pressure in the analytic vacuum chamber was less than 10^{-10} Torr for all performed measurements.

Conclusion

Our comprehensive study of $Mn_{1-x}Ge_xBi_2Te_4$ single crystals with varying Ge concentrations has provided significant insights into the evolution of their electronic structure. Through detailed ARPES measurements, we have observed a clear correlation between the Ge concentration and the bulk band gap behavior. Specifically, as the Ge concentration x increases up to approximately 40%, the bulk band gap decreases to zero, indicating a TPT.

Within this concentration range, the TSS are well visible, but their intensity gradually decreases with increasing Ge concentration; they disappear completely as the Ge content continues to increase. The band gap is assumed to be zero for

concentrations between 45–60% due to the presence of the ARPES signal in the DP region from the bulk Ge-contributed states. Further increases in Ge concentration result in a corresponding increase in the band gap, as the $Mn_{1-x}Ge_xBi_2Te_4$ system with high x behaves more like Mn-doped $GeBi_2Te_4$, where the band gap is finite. These bulk Ge-contributed states also manifest as Rashba-like bands that lower their energy with increasing Ge concentration. Finally, TrSS, exhibiting an energy splitting of 70–100 meV (measured by different methods), remain constant for Ge concentrations of 45–60%.

DFT electronic structure calculations of 12 SL-thick slabs and bulk primitive cells of $Mn_{1-x}Ge_xBi_2Te_4$ with varying Ge concentrations also show that the bulk band gap decreases as the Ge concentration increases and reaches zero values when Ge concentrations are in the 33–50% range. With further increases in Ge concentration above 60%, the bulk gap reopens. Bulk-projected band calculations also confirm the formation of a zero-gap plateau. Furthermore, DFT calculation results confirm that the band dispersions display the presence of Rashba-like surface states in addition to TSS, which shift towards higher binding energies with increasing Ge concentration. These states hybridize with conduction bands and exhibit energy splitting of approximately 100 and 70 meV, which remains stable in the concentration range of 45–60%.

To analyze the possibility and reasons for the formation of a plateau with a minimum band gap, as well as to explore the potential for forming the state of a magnetic WSM in this system, comparative calculations of changes in the electronic structure in the AFM and FM phases were carried out. These calculations varied both the concentration of Ge and the modulation of the SOC strength and interplanar distance (through expansion and contraction of the system). The results showed that for the FM phase, the TPT from the TI state to the trivial insulator (TrivIns) state does not occur directly. Instead, it proceeds through a sequence of topological transformations: from the TI phase through the DSM state to the WSM phase (with the intersection of states in the ΓZ direction) and then to the TrivIns phase, again through the DSM state (TI—DSM–WSM–DSM–TrivIns). This sequence of TPTs suggests the possibility of forming a plateau in the dependence of the band gap size, as observed in the experiment. In contrast, for the AFM phase, calculations of the dependence of the electronic structure on the SOC strength modulation and interplanar distance do not show the presence of such a plateau with a minimum band gap. Instead, they show only the TPT from the AFM TI to the TrivIns state through the DSM phase in a single-point transition.

Based on these calculations, we assumed that the presence of the plateau in the experimental dependence of the band gap in the Ge concentration range of 35–50% can be determined by the local transition of part of the sample to the WSM state (presumably with local ferrimagnetic ordering), which ensures the formation of a plateau with an apparent zero bulk gap in the region of these concentrations. To test this assumption, model calculations were carried out, which confirmed the possibility of a transition to the state of a magnetic WSM directly from an AFM TI under the condition of local disruption of magnetic ordering by the replacement of Mn atoms by Ge not in every Mn layer, but through the layer. This condition creates the maximum possible local violation of the AFM-type interaction. In this case, the electronic structure acquires the features characteristic of the state of a magnetic WSM without the need for external remagnetization of the system.

Acknowledgements

This work was supported by the Russian Science Foundation grant No. 23-12-00016 and the St. Petersburg State University grant No. 95442847. HiSOR ARPES measurements were performed under Proposals No. 23AG008, 23AU003, 23AU012, 23BU003. We are grateful to the N-BARD, Hiroshima University for liquid He supplies. The $Mn_{1-x}Ge_xBi_2Te_4$ single crystals were grown using the Bridgeman method under state assignment of Sobolev Institute of Geology and Mineralogy SB RAS #122041400031-2. The project that gave rise to these results received the support of a fellowship from “la Caixa” Foundation (ID 100010434). O.E.T. and V.A.G. acknowledge RSF No. 22-12-20024 (p-9) in the part of the XPS calibration of stoichiometry for ARPES measurements with using He lamp at ISP SB RAS. The calculations were partially performed using the equipment of the Joint Supercomputer Center of the Russian Academy of Sciences (https://rscgroup.ru/en/project/jscc). The authors acknowledge SPbU Research Park “Physical Methods of Surface Investigation” and “Nanotechnology” where the elemental composition of studied samples was investigated.

Author contributions statement

The manuscript was written and edited by A.M. Shikin, A.V. Tarasov, and A.V. Eryzhenkov. All co-authors took part in the discussion and analysis of the experimental results. Preparation of the manuscript for publication, including the presentation of the figures, was carried out by A.V. Tarasov and T.P. Estyunina. ARPES measurements with He Iα radiation were conducted by A.M. Shikin, D.A. Estyunin, T.P. Estyunina, V.A. Golyashov and O.E. Tereshchenko. ARPES measurements with with laser radiation (μ-ARPES and SpinLaser ARPES) were conducted by A.M. Shikin, D.A. Estyunin, T.P. Estyunina, A.G. Rybkin, I.I. Klimovskikh, S. Ideta, Y. Miyai, Y. Kumar, T. Iwata, T. Kosa, K. Kuroda and K. Shimada. Experimental data processing was handled by D.A. Glazkova, T.P. Estyunina and D.A. Estyunin. The band structure calculations were carried out by A.V. Tarasov, N.L. Zaitsev, and T.P. Estyunina. Crystals were grown by K.A. Kokh and O.E. Tereshchenko. All authors reviewed the manuscript. The project was planned and supervised by A.M. Shikin.

Competing Interests

The authors declare no competing interests.

Data Availability

All data generated or analysed during this study are included in this published article (and its Supplementary Information files).

Additional information

Supplementary Information The online version contains supplementary material.

References

1. Qi, X.-L., Hughes, T. L. & Zhang, S.-C. Topological field theory of time-reversal invariant insulators. *Phys. Rev. B* **78**, 195424, DOI: 10.1103/PhysRevB.78.195424 (2008).
2. Qi, X.-L. & Zhang, S.-C. Topological insulators and superconductors. *Rev. Mod. Phys.* **83**, 1057–1110, DOI: 10.1103/RevModPhys.83.1057 (2011).
3. Sekine, A. & Nomura, K. Axion electrodynamics in topological materials. *J. Appl. Phys.* **129**, 141101, DOI: 10.1063/5.0038804 (2021).
4. Chang, C.-Z., Liu, C.-X. & MacDonald, A. H. Colloquium: Quantum anomalous Hall effect. *Rev. Mod. Phys.* **95**, 011002, DOI: 10.1103/RevModPhys.95.011002 (2023).
5. Tokura, Y., Yasuda, K. & Tsukazaki, A. Magnetic topological insulators. *Nat. Rev. Phys.* **1**, 126–143, DOI: 10.1038/s42254-018-0011-5 (2019).
6. Wang, P. *et al.* Intrinsic magnetic topological insulators. *The Innov.* **2**, 100098, DOI: https://doi.org/10.1016/j.xinn.2021.100098 (2021).
7. He, Q. L., Hughes, T. L., Armitage, N. P., Tokura, Y. & Wang, K. L. Topological spintronics and magnetoelectronics. *Nat. Mater.* **21**, 15–23, DOI: 10.1038/s41563-021-01138-5 (2022).
8. Gilbert, M. J. Topological electronics. *Commun. Phys.* **4**, 70, DOI: 10.1038/s42005-021-00569-5 (2021).
9. Rienks, E. D. L. *et al.* Large magnetic gap at the dirac point in bi2te3/mnbi2te4 heterostructures. *Nature* **576**, 423–428, DOI: 10.1038/s41586-019-1826-7 (2019).
10. Otrokov, M. M. *et al.* Prediction and observation of an antiferromagnetic topological insulator. *Nature* **576**, 416–422, DOI: 10.1038/s41586-019-1840-9 (2019).
11. Aliev, Z. S. *et al.* Novel ternary layered manganese bismuth tellurides of the $MnTe - Bi_2Te_3$ system: Synthesis and crystal structure. *J. Alloy. Compd.* **789**, 443–450, DOI: https://doi.org/10.1016/j.jallcom.2019.03.030 (2019).
12. Li, J. *et al.* Intrinsic magnetic topological insulators in van der Waals layered $MnBi_2Te_4$-family materials. *Sci. Adv.* **5**, eaaw5685, DOI: 10.1126/sciadv.aaw5685 (2019).
13. Zhang, D. *et al.* Topological axion states in the magnetic insulator $MnBi_2Te_4$ with the quantized magnetoelectric effect. *Phys. Rev. Lett.* **122**, 206401, DOI: 10.1103/PhysRevLett.122.206401 (2019).
14. Gong, Y. *et al.* Experimental realization of an intrinsic magnetic topological insulator. *Chin. Phys. Lett.* **36**, 076801, DOI: 10.1088/0256-307X/36/7/076801 (2019).
15. Estyunin, D. A. *et al.* Signatures of temperature driven antiferromagnetic transition in the electronic structure of topological insulator $MnBi_2Te_4$. *APL Mater.* **8**, 021105, DOI: 10.1063/1.5142846 (2020). https://pubs.aip.org/aip/apm/article-pdf/doi/10.1063/1.5142846/14563355/021105_1_online.pdf.
16. Shikin, A. M. *et al.* Sample-dependent Dirac-point gap in $MnBi_2Te_4$ and its response to applied surface charge: A combined photoemission and *ab initio* study. *Phys. Rev. B* **104**, 115168, DOI: 10.1103/PhysRevB.104.115168 (2021).
17. Shikin, A. M. *et al.* Nature of the Dirac gap modulation and surface magnetic interaction in axion antiferromagnetic topological insulator $MnBi_2Te_4$. *Sci. Reports* **10**, 13226, DOI: 10.1038/s41598-020-70089-9 (2020).
18. Shikin, A. M. *et al.* Modulation of the Dirac point band gap in the antiferromagnetic topological insulator $MnBi_2Te_4$ due to the surface potential gradient change. *J. Exp. Theor. Phys.* **134**, 103–111, DOI: 10.1134/S1063776121120141 (2022).

19. Garnica, M. *et al.* Native point defects and their implications for the Dirac point gap at $MnBi_2Te_4$ (0001). *npj Quantum Mater.* **7**, 7, DOI: 10.1038/s41535-021-00414-6 (2022).

20. Shikin, A. *et al.* Routes for the topological surface state energy gap modulation in antiferromagnetic $MnBi_2Te_4$. *Phys. B: Condens. Matter* **649**, 414443, DOI: 10.1016/j.physb.2022.414443 (2023).

21. Eremeev, S. V. *et al.* Topological magnetic materials of the $(MnSb_2Te_4)\cdot(Sb_2Te_3)_n$ van der Waals compounds family. *The J. Phys. Chem. Lett.* **12**, 4268–4277, DOI: 10.1021/acs.jpclett.1c00875 (2021).

22. Klimovskikh, I. I. *et al.* Tunable 3D/2D magnetism in the $(MnBi_2Te_4)(Bi_2Te_3)_m$ topological insulators family. *npj Quantum Mater.* **5**, 54, DOI: 10.1038/s41535-020-00255-9 (2020).

23. Shikin, A. M., Estyunin, D. A., Glazkova, D. A., Fil'nov, S. O. & Klimovskikh, I. I. Electronic and spin structures of intrinsic antiferromagnetic topological insulators of the $MnBi_2Te_4(Bi_2Te_3)_m$ family and their magnetic properties (brief review). *JETP Lett.* **115**, 213–225, DOI: 10.1134/S0021364022040117 (2022).

24. Deng, Y. *et al.* Quantum anomalous Hall effect in intrinsic magnetic topological insulator $MnBi_2Te_4$. *Science* **367**, 895–900, DOI: 10.1126/science.aax8156 (2020).

25. Liu, C. *et al.* Robust axion insulator and Chern insulator phases in a two-dimensional antiferromagnetic topological insulator. *Nat. Mater.* **19**, 522–527, DOI: 10.1038/s41563-019-0573-3 (2020).

26. Deng, H. *et al.* High-temperature quantum anomalous Hall regime in a $MnBi_2Te_4/Bi_2Te_3$ superlattice. *Nat. Phys.* **17**, 36–42, DOI: 10.1038/s41567-020-0998-2 (2021).

27. Gao, A. *et al.* Layer Hall effect in a 2D topological axion antiferromagnet. *Nature* **595**, 521–525, DOI: 10.1038/s41586-021-03679-w (2021).

28. Li, S. *et al.* Progress on the antiferromagnetic topological insulator $MnBi_2Te_4$. *Natl. Sci. Rev.* **11**, nwac296, DOI: 10.1093/nsr/nwac296 (2023).

29. Hao, Y.-J. *et al.* Gapless surface Dirac cone in antiferromagnetic topological insulator $MnBi_2Te_4$. *Phys. Rev. X* **9**, 041038, DOI: 10.1103/PhysRevX.9.041038 (2019).

30. Chen, Y. J. *et al.* Topological electronic structure and its temperature evolution in antiferromagnetic topological insulator $MnBi_2Te_4$. *Phys. Rev. X* **9**, 041040, DOI: 10.1103/PhysRevX.9.041040 (2019).

31. Swatek, P. *et al.* Gapless Dirac surface states in the antiferromagnetic topological insulator $MnBi_2Te_4$. *Phys. Rev. B* **101**, 161109, DOI: 10.1103/PhysRevB.101.161109 (2020).

32. Chowdhury, S., Garrity, K. F. & Tavazza, F. Prediction of Weyl semimetal and antiferromagnetic topological insulator phases in Bi_2MnSe_4. *npj Comput. Mater.* **5**, 33, DOI: 10.1038/s41524-019-0168-1 (2019).

33. Zhang, H., Yang, W., Wang, Y. & Xu, X. Tunable topological states in layered magnetic materials of $MnSb_2Te_4$, $MnBi_2Se_4$, and $MnSb_2Se_4$. *Phys. Rev. B* **103**, 094433, DOI: 10.1103/PhysRevB.103.094433 (2021).

34. Zhou, L. *et al.* Topological phase transition in the layered magnetic compound $MnSb_2Te_4$: Spin-orbit coupling and interlayer coupling dependence. *Phys. Rev. B* **102**, 085114, DOI: 10.1103/PhysRevB.102.085114 (2020).

35. Tarasov, A. V. *et al.* Topological phase transitions driven by Sn doping in $(Mn_{1-x}Sn_x)Bi_2Te_4$. *Symmetry* **15**, DOI: 10.3390/sym15020469 (2023).

36. Estyunina, T. P. *et al.* Evolution of $Mn_{1-x}Ge_xBi_2Te_4$ electronic structure under variation of Ge content. *Nanomaterials* **13**, DOI: 10.3390/nano13142151 (2023).

37. Frolov, A. S. *et al.* Magnetic Dirac semimetal state of $(Mn,Ge)Bi_2Te_4$. *Commun. Phys.* **7**, 180, DOI: 10.1038/s42005-024-01675-w (2024).

38. Qian, T. *et al.* Magnetic dilution effect and topological phase transitions in $(Mn_{1-x}Pb_x)Bi_2Te_4$. *Phys. Rev. B* **106**, 045121, DOI: 10.1103/PhysRevB.106.045121 (2022).

39. Changdar, S. *et al.* Nonmagnetic Sn doping effect on the electronic and magnetic properties of antiferromagnetic topological insulator $MnBi_2Te_4$. *Phys. B: Condens. Matter* **657**, 414799, DOI: https://doi.org/10.1016/j.physb.2023.414799 (2023).

40. Zhu, J. *et al.* Magnetic and electrical transport study of the antiferromagnetic topological insulator Sn-doped $MnBi_2Te_4$. *Phys. Rev. B* **103**, 144407, DOI: 10.1103/PhysRevB.103.144407 (2021).

41. Yan, J.-Q. Perspective: The elusive quantum anomalous Hall effect in $MnBi_2Te_4$: Materials. *ECS J. Solid State Sci. Technol.* **11**, 063007, DOI: 10.1149/2162-8777/ac70fc (2022).

42. Estyunin, D. A. *et al.* Comparative study of magnetic properties of $(Mn_{1-x}A^{IV}_x)Bi_2Te_4$, $A^{IV} = Ge, Pb, Sn$. *Magnetochemistry* **9**, DOI: 10.3390/magnetochemistry9090210 (2023).

43. Armitage, N. P., Mele, E. J. & Vishwanath, A. Weyl and Dirac semimetals in three-dimensional solids. *Rev. Mod. Phys.* **90**, 015001, DOI: 10.1103/RevModPhys.90.015001 (2018).

44. Li, J. *et al.* Magnetically controllable topological quantum phase transitions in the antiferromagnetic topological insulator $MnBi_2Te_4$. *Phys. Rev. B* **100**, 121103, DOI: 10.1103/PhysRevB.100.121103 (2019).

45. Lv, B. Q., Qian, T. & Ding, H. Experimental perspective on three-dimensional topological semimetals. *Rev. Mod. Phys.* **93**, 025002, DOI: 10.1103/RevModPhys.93.025002 (2021).

46. Hasan, M. *et al.* Weyl, Dirac and high-fold chiral fermions in topological quantum matter. *Nat. Rev. Mater.* **6**, 784–803, DOI: 10.1038/s41578-021-00301-3 (2021).

47. Guan, S. *et al.* Artificial gravity field, astrophysical analogues, and topological phase transitions in strained topological semimetals. *npj Quantum Mater.* **2**, 23, DOI: 10.1038/s41535-017-0026-7 (2017).

48. Wang, Y. Chemical requirements for stabilizing type-II Weyl points in $MnBi_{2-x}Sb_xTe_4$, DOI: 10.48550/ARXIV.2103.12730 (2021). 2103.12730.

49. Vidal, R. C. *et al.* Surface states and Rashba-type spin polarization in antiferromagnetic $MnBi_2Te_4(0001)$. *Phys. Rev. B* **100**, 121104, DOI: 10.1103/PhysRevB.100.121104 (2019).

50. Niu, C. *et al.* Realization of tunable dirac cone and insulating bulk states in topological insulators (bi1xsbx)2te3. *Sci. Reports* **2**, 976, DOI: 10.1038/srep00976 (2012).

51. Golyashov, V. A., Kokh, K. A. & Tereshchenko, O. E. Transport properties of $(Bi, Sb)_2te_3$ topological insulator crystals with lateral p-n junction. *Phys. Rev. Mater.* **7**, 124204, DOI: 10.1103/PhysRevMaterials.7.124204 (2023).

52. Iwasawa, H. *et al.* Development of laser-based scanning μ-ARPES system with ultimate energy and momentum resolutions. *Ultramicroscopy* **182**, 85–91, DOI: https://doi.org/10.1016/j.ultramic.2017.06.016 (2017).

53. Iwata, T. *et al.* Laser-based angle-resolved photoemission spectroscopy with micrometer spatial resolution and detection of three-dimensional spin vector. *Sci. Reports* **14**, 127, DOI: 10.1038/s41598-023-47719-z (2024).

54. Shikin, A. M., Estyunina, T. P., Eryzhenkov, A. V., Zaitsev, N. L. & Tarasov, A. V. Topological phase transition in the antiferromagnetic topological insulator $MnBi_2Te_4$ from the point of view of axion-like state realization. *Sci. Reports* **13**, 16343, DOI: 10.1038/s41598-023-42466-7 (2023).

55. Xu, S.-Y. *et al.* Observation of Fermi arc surface states in a topological metal. *Science* **347**, 294–298, DOI: 10.1126/science.1256742 (2015).

56. Wang, Z. *et al.* Dirac semimetal and topological phase transitions in A_3Bi ($A = Na, K, Rb$). *Phys. Rev. B* **85**, 195320, DOI: 10.1103/PhysRevB.85.195320 (2012).

57. Li, P., Yu, J., Wang, Y. & Luo, W. Electronic structure and topological phases of the magnetic layered materials $MnBi_2Te_4$, $MnBi_2Se_4$, and $MnSb_2Te_4$. *Phys. Rev. B* **103**, 155118, DOI: 10.1103/PhysRevB.103.155118 (2021).

58. Murakami, T. *et al.* Realization of interlayer ferromagnetic interaction in $MnSb_2Te_4$ toward the magnetic Weyl semimetal state. *Phys. Rev. B* **100**, 195103, DOI: 10.1103/PhysRevB.100.195103 (2019).

59. Liu, Y. *et al.* Site mixing for engineering magnetic topological insulators. *Phys. Rev. X* **11**, 021033, DOI: 10.1103/PhysRevX.11.021033 (2021).

60. Wimmer, S. *et al.* Mn-rich $MnSb_2Te_4$: A topological insulator with magnetic gap closing at high Curie temperatures of 45–50 K. *Adv. Mater.* **33**, 2102935, DOI: https://doi.org/10.1002/adma.202102935 (2021).

61. Liu, J. & Vanderbilt, D. Weyl semimetals from noncentrosymmetric topological insulators. *Phys. Rev. B* **90**, 155316, DOI: 10.1103/PhysRevB.90.155316 (2014).

62. Burkov, A. A. & Balents, L. Weyl semimetal in a topological insulator multilayer. *Phys. Rev. Lett.* **107**, 127205, DOI: 10.1103/PhysRevLett.107.127205 (2011).

63. Yang, Y. *et al.* Time-reversal-symmetry-broken quantum spin Hall effect. *Phys. Rev. Lett.* **107**, 066602, DOI: 10.1103/PhysRevLett.107.066602 (2011).

64. Ozaki, T. Variationally optimized atomic orbitals for large-scale electronic structures. *Phys. Rev. B* **67**, 155108, DOI: 10.1103/PhysRevB.67.155108 (2003).

65. Ozaki, T. & Kino, H. Numerical atomic basis orbitals from H to Kr. *Phys. Rev. B* **69**, 195113, DOI: 10.1103/PhysRevB.69.195113 (2004).

66. Ozaki, T. & Kino, H. Efficient projector expansion for the *ab initio* LCAO method. *Phys. Rev. B* **72**, 045121, DOI: 10.1103/PhysRevB.72.045121 (2005).

67. Troullier, N. & Martins, J. L. Efficient pseudopotentials for plane-wave calculations. *Phys. Rev. B* **43**, 1993–2006, DOI: 10.1103/PhysRevB.43.1993 (1991).

68. Perdew, J. P., Burke, K. & Ernzerhof, M. Generalized gradient approximation made simple. *Phys. Rev. Lett.* **77**, 3865–3868, DOI: 10.1103/PhysRevLett.77.3865 (1996).

69. Han, M. J., Ozaki, T. & Yu, J. $O(n)$ LDA $+U$ electronic structure calculation method based on the nonorthogonal pseudoatomic orbital basis. *Phys. Rev. B* **73**, 045110, DOI: 10.1103/PhysRevB.73.045110 (2006).

70. Dudarev, S. L., Botton, G. A., Savrasov, S. Y., Humphreys, C. J. & Sutton, A. P. Electron-energy-loss spectra and the structural stability of nickel oxide: An LSDA+U study. *Phys. Rev. B* **57**, 1505–1509, DOI: 10.1103/PhysRevB.57.1505 (1998).